



Enhancing volumetric muscle loss (VML) recovery in a rat model using super durable hydrogels derived from bacteria

Seyyed Vahid Niknezhad^{a,1}, Mehdi Mehrali^{b,1,**}, Farinaz Riyahi Khorasgani^c, Reza Heidari^d,
Firoz Babu Kadumudi^c, Nasim Golafshan^{c,e}, Miguel Castilho^{f,k}, Cristian Pablo Pennisi^g,
Masoud Hasany^b, Mohammadjavad Jahanshahi^h, Mohammad Mehraliⁱ, Younes Ghasemi^d,
Negar Azarpira^j, Thomas L. Andresen^l, Alireza Dolatshahi-Pirouz^{c,*}

^a Burn and Wound Healing Research Center, Shiraz University of Medical Sciences, Shiraz, 71987-54361, Iran

^b Department of Civil and Mechanical Engineering, Technical University of Denmark, 2800, Kgs Lyngby, Denmark

^c Department of Health Technology, Technical University of Denmark, 2800, Kongens Lyngby, Denmark

^d Pharmaceutical Sciences Research Center, Shiraz University of Medical Sciences, Shiraz, Iran

^e Department of Orthopaedics, University Medical Center Utrecht, Utrecht, 3584 CX, the Netherlands

^f Department of Biomedical Engineering, Eindhoven University of Technology, the Netherlands

^g Regenerative Medicine Group, Department of Health Science and Technology, Aalborg University, 9260, Gistrup, Denmark

^h Department of Chemistry, Faculty of Science, University of Jiroft, 8767161167, Jiroft, Iran

ⁱ Faculty of Engineering Technology, Department of Thermal and Fluid Engineering (TFE), University of Twente, 7500 AE, Enschede, the Netherlands

^j Transplant Research Center, Shiraz University of Medical Sciences, Shiraz, Iran

^k Institute for Complex Molecular Systems, Eindhoven University of Technology, Eindhoven, the Netherlands

^l Department of Health Technology, Section for Biotherapeutic Engineering and Drug Targeting, Technical University of Denmark, 2800, Kongens Lyngby, Denmark

ABSTRACT

Bacteria can be programmed to deliver natural materials with defined biological and mechanical properties for controlling cell growth and differentiation. Here, we present an elastic, resilient and bioactive polysaccharide derived from the extracellular matrix of *Pantoea* sp. BCCS 001. Specifically, it was methacrylated to generate a new photo crosslinkable hydrogel that we coined Pantoan Methacrylate or put simply PAMA. We have used it for the first time as a tissue engineering hydrogel to treat VML injuries in rats. The crosslinked PAMA hydrogel was super elastic with a recovery nearing 100 %, while mimicking the mechanical stiffness of native muscle. After inclusion of thiolated gelatin via a Michaelis reaction with acrylate groups on PAMA we could also guide muscle progenitor cells into fused and aligned tubes – something reminiscent of mature muscle cells. These results were complemented by sarcomeric alpha-actinin immunostaining studies. Importantly, the implanted hydrogels exhibited almost 2-fold more muscle formation and 50 % less fibrous tissue formation compared to untreated rat groups. *In vivo* inflammation and toxicity assays likewise gave rise to positive results confirming the biocompatibility of this new biomaterial system. Overall, our results demonstrate that programmable polysaccharides derived from bacteria can be used to further advance the field of tissue engineering. In greater detail, they could in the foreseeable future be used in practical therapies against VML.

1. Introduction

Volumetric muscle loss (VML) from injury or disease results in almost \$400 billion in healthcare expenses every year in the USA alone [1]. Even though, healthy muscle can regenerate itself for the most part, it is unable to fully repair when the tissue loss is volumetric and exceeds 20 % of the muscle weight. Instead, the new muscle tissue will consist of non-functional fatty tissue and fibrous scar tissue formation [2,3]. To

this end, conventional strategies aim at using autologous muscle grafts for restoring muscle function. However, autografting is limited by tissue availability, suboptimal regeneration, postoperative infection, scar tissue formation, and donor site morbidity [4]. A facile strategy to counterweigh this daunting challenge revolves around putting tissue engineering to work. Until now, these treatments have unlocked better vascularization, force production and tissue formation – however, there is still some ground to cover before reaching complete tissue restoration

Peer review under responsibility of KeAi Communications Co., Ltd.

* Corresponding author.

** Corresponding author.

E-mail addresses: meme@dtu.dk (M. Mehrali), aldo@dtu.dk (A. Dolatshahi-Pirouz).

¹ Equal contribution.

<https://doi.org/10.1016/j.bioactmat.2024.04.006>

Received 10 October 2023; Received in revised form 12 March 2024; Accepted 8 April 2024

2452-199X/© 2024 The Authors. Publishing services by Elsevier B.V. on behalf of KeAi Communications Co. Ltd. This is an open access article under the CC BY-NC-ND license (<http://creativecommons.org/licenses/by-nc-nd/4.0/>).

after VML injury [5].

The classical tissue engineering approach encompasses *in vitro* expansion of cells and subsequent seeding on porous biomaterials (scaffolds) [6]. They can either become implanted directly or cultured in a bioreactor to yield more mature tissue constructs. Unfortunately, the concept has been facing serious challenges, which is delaying the fulfillment of its promise. These mainly include the laborious time and effort that goes into the cell expansion and seeding phase, in combination with a lack of a renewable cell sources and the difficult path towards clinical approval for using laboratory grown cells in humans. Thus, *in situ* tissue engineering has gained increasing attention [7–11]. In this simple approach, implanted biomaterials use the body's own regenerative capacity through recruitment and controlled stimulation of native stem/progenitor cells typically within 3D native matrices or on bioactive coatings to achieve the best outcomes. This approach has already been used for vascular grafts, nerve, muscle, and hard tissue engineering with promising outcomes.

To this end, hydrogels display an impressive track-record due to their ability to facilitate efficient exchange of nutrients and waste products with the surrounding environment, muscle-like stiffness, injectability, and native-like biological properties resembling those of the extracellular matrix (ECM) [12,13]. They can both be used to deliver cells and act as artificial microenvironments that can put our bodies own cells to work – all accomplished via minimal invasive routes paved away by their injectability. Along these lines several recent studies have shown that hydrogels provide a favorable milieu for migrating satellite muscle cells [14,15]. For these reasons they are at the very heart of the field. However, commercially available hydrogels are not dynamic, and simultaneously limited by their subpar mechanical stiffness, low durability, rapid degradation [16–18]. Indeed, human tissues are highly responsive and dynamic – for this reason a perfect merger between artificial systems and organs require time-dependent systems capable of reconfiguring and evolving inside the body [19].

In this direction the exopolymeric substances (EPS) obtained from bacterial biofilms are good candidates as they are both resilient, programmable, and scalable. In greater detail, bacteria can convert carbon and nitrogen sources into a great variety of biomolecules [20]. Some of these including cellulose, hyaluronate, levan, gellan, alginate, bioactive peptides and amyloid fibers, which have been used to generate highly versatile and programmable hydrogels. Biomaterial engineers have in recent years used them in combination with synthetic biology to create living biofilm-based materials mimicking biological features including self-healing, self-growth and responsiveness to various microenvironmental factors [21–26]. This explains why hydrogels made from bacterial components have become paradigm breakers in the world of material science. For instance, recent studies have utilized pellicles created by cellulose-producing bacteria as self-healing systems and living bioinks capable of self-growth [27]. Some of these have been engineered to become biosensors that can sense external stimuli and subsequently respond with a pre-defined change in gene expression. Others have focused on functional biofilm-based amyloids for the manufacture of self-regenerating hydrogels that can interact with different parts of the gastrointestinal tract in a programmable manner [26]. In a similar study by the same group, they leveraged on the same microbial engineering principles and delivered smart 3D printed living systems capable of eliminating toxic elements from the environment, controlled drug release and self-regulated growth [22].

Here, we have methacrylated a bacteria-derived EPS to open a new and exciting avenue in the search of the next groundbreaking hydrogel system. The bacteria strain we investigated, known as *Pantoea* sp. BCCS 001 GH, was isolated from nectarine fruit. Bacteria employ EPS as a defense mechanism against various physical stress factors – for this reason they need to be sufficiently tough and resilient. The *pantoea* EPS strain investigated in this study achieved exceptional mechanical properties due to its unique triple helical structure held together by reversible hydrogen bonds and hydrophobic interactions. Overall, we

could successfully cross-link the methacrylated hydrogel system via UV-light and fine-tune the mechanical properties in the range 5 kPa–15 kPa similar to that of the native muscle ECM. Notably, the material was super elastic, as it was compressible up to 70 % with a recovery rate close to 100 %. By including thiolated gelatin into the backbone via a Michaelis reaction we could even achieve native-like bioactivity resulting in fused and aligned muscle progenitor cells - this is considered by many laymen engineers in the field as important maturity indicators. Finally, we investigated the performance of the photo-crosslinked gels in a rat model of VML and found significant differences in both muscle and fibrous formation capacity – with the gelatin incorporated hydrogels outperforming all other groups. In summary, we have presented a new novel route for cost-effective manufacture of biocompatible hydrogel systems mimicking both the mechanical and biological properties of muscle tissue. Based on our *in vivo* results we envision them within the foreseeable as promising candidates for treating severe VML cases.

2. Results

Pantoan extracted from *sp.* BCCS 001 GH is composed of glucose and galactose units in the D-configuration with a glucose/galactose ratio of approximately 85.18:14.82 and a molecular weight of 2400 kDa [28]. The molecule therefore contains plenty of carboxyl groups that we can activate via the carbodiimide (EDC) and *N*-hydroxysuccinimide (NHS) methods to make them reactive towards methacrylate groups. We could therefore via readily accessible chemical protocols transform Pantoan to Pantoan Methacrylate (PAMA) and incorporate thiolated gelatin (Gel-in-S) into its structure through a Michaelis reaction between thiol and acrylate groups. The EPS strain used in this study also exhibits a unique triple helical structure held together by reversible hydrogen bonds and hydrophobic interactions [29]. Indeed, such reversible linkages are paradigm breakers in the field because of their ability to dissipate energy reversibly and continuously, thereby increasing the fracture energy. This can ultimately result in high material elasticity and durability. We have characterized this new and novel hydrogel system chemically, mechanically, and biologically in the following sections. Notably, we have carried out extensive *in vivo* studies in a VML rat model for up to 21 days.

2.1. Chemical characterization

Pantoan methacrylate (PAMA) with various degrees of methacrylation was synthesized by substituting the hydroxyl groups of Pantoan with methacrylate groups (Fig. 1a) to engineer. The amount of methacrylic anhydride added to the reaction mixture was varied to control the methacrylation degree. The introduction of methacrylate groups makes PAMA easy to crosslink upon UV exposure, since PAMA is otherwise non-crosslinkable, which is confirmed by the gelation phenomenon of the aqueous solution of PAMA upon UV irradiation at 365 nm (Fig. 1b). Further, we examined if the methacrylation of pantoan was successful by analyzing the net surface charge in terms of zeta potential measurements (Fig. 1c). In general, polysaccharides exhibit large negative net surface charges due to the numerous hydroxyl groups in their backbone. Similarly, the extracted pantoan also carries a high amount of hydroxyl groups, resulting in a very high negative zeta potential value of -50 mV at pH 7. On the other hand, methacrylate groups are positive and should therefore in theory reduce the negative charge. Indeed, as expected, the substitution of positive methacrylate groups slightly reduced the zeta potentials values to -40 mV and -37 mV for PAMA₂₁ and PAMA₃₇ samples, respectively.

The inclusion of methacrylate groups into the pantoan backbone was further confirmed by Proton nuclear magnetic resonance (¹HNMR) spectroscopic analysis (Fig. 1d). Here, the presence of methacryloyl groups at $\delta = 5.8$ and 6.2 ppm corresponds to vinyl groups, and the peak at $\delta = 1.9$ ppm corresponds to methyl ($-CH_3$) groups confirming the methacrylation of hydroxyl groups in the pantoan backbone [30,31]. We

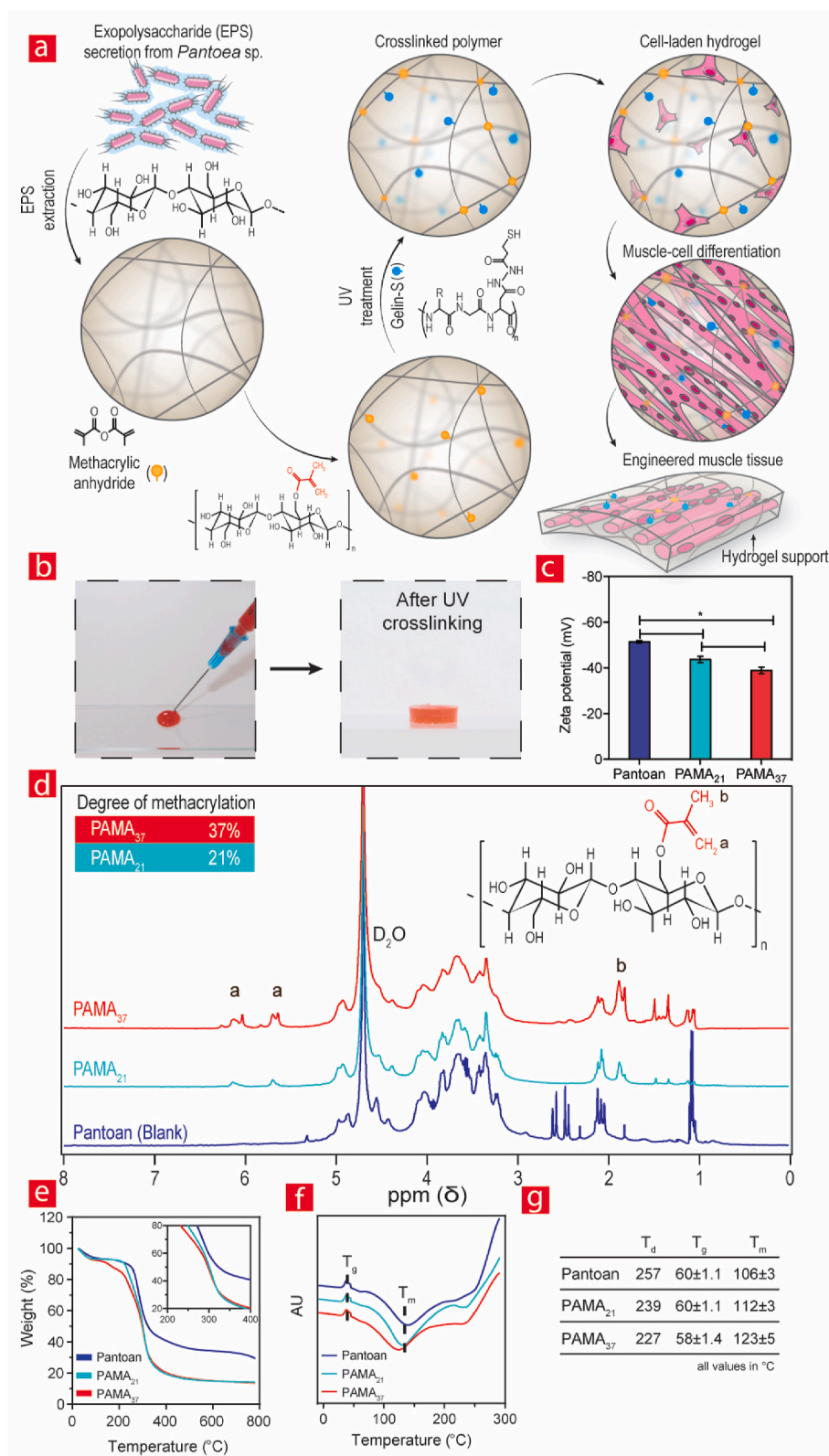


Fig. 1. Chemistry behind the developed hydrogels and the corresponding characterizations. (a) Chemical structure of pantoan before and after methacrylation. (b) Photographic images of PAMA before and after UV cross-linking. (c) Zeta potential measurements of pantoan and PAMA with two methacrylation degrees. (d) Nuclear magnetic resonance (NMR) spectroscopy of pantoan and PAMA with different methacrylation degrees. (e–g) The thermal stability and crystallization temperature of pantoan and PAMA₂₁ and PAMA₃₇ were examined with TGA and DSC.

calculated the degree of methacrylation by comparing the intensity of CH₃ proton at 1.9 ppm of the methacrylate and proton signals at 4.4 from the H-4 position of the pantoan molecule. The calculated methacrylation degree for 1.5 mL and 2.5 mL methacrylic anhydride was 21% and 37%, respectively. Further, methacrylation of the pantoan was confirmed by Fourier transform infrared (FTIR) spectroscopic analysis (Supplementary Fig. 1a). Specifically, the appearance of new peaks at 1660, 1455, and 898 cm⁻¹ in the PAMA₂₁ and PAMA₃₇ backbone corresponding to C=C, =CH₂, and =CH bonds, respectively, confirm the covalent bond formation between pantoan and methacrylate groups [30, 31]. In addition, the interaction of PAMA₂₁ with Gelin-S after UV crosslinking was also confirmed by FTIR analysis (Supplementary Fig. 1a). Upon crosslinking, thiol-ene Michael addition occurs between the thiol group present in the Gelin-S and methacrylate groups in the PAMA₂₁, which is confirmed by the disappearance of the thiol group at 2450 cm⁻¹ and acrylate groups at 898 cm⁻¹ in the FTIR spectra of crosslinked PAMA₂₁-Gelin-S samples.

Finally, the thermal properties of PAMA₂₁ were analyzed using TGA and DSC analysis (Fig. 1 e). The pantoan polysaccharide before and after methacrylation showed an 8% weight loss below 200 °C - something correlated with the removal of water moisture. The onset temperature for thermal degradation of pantoan (257 °C) was decreased to lower temperatures after methacrylation due to the loss of intermolecular hydrogen bonding between hydroxyl groups present in the backbone of adjacent polysaccharides [32,33]. Similarly, the DSC analysis exhibited a broad endothermic transitions in the temperature range of 75–200 °C attributed to the desorption of water molecules and the melting of semi-crystalline segments. A further endothermic transition was observed between 200 and 250 °C (Fig. 1f and g), corresponding to the melting of crystalline regions within the EPS. Upon methacrylation of the EPS, a notable transformation was observed in the semi-crystalline polymer. This modification led to an elevation of the melting temperature peaks from 106 °C (for the unmodified Pantoan) to 123 °C [34–36]. Accompanying this shift, a reduction in the enthalpy change from -285.8 J/g to -237.9 J/g was observed for melting of semi-crystalline segments ($\Delta H_{\text{semi-cryst.}}$). At the same time, the enthalpy changes of the crystalline regions ($\Delta H_{\text{cryst.}}$) decreased from -14.3 J/g to -8.6 J/g (Supplementary Table S1). This reduction signifies the successful methacrylation of the Pantoan polysaccharide and indicates that the methacrylation process decreases the crystallinity of pristine Pantoan. By decreasing the number of hydroxyl groups available for hydrogen bonding as these are one of the most important driving forces behind higher-order structures in polymers. Furthermore, following the thiol-ene Michael addition reaction with Gelin-S, the TGA of PAMA₂₁-Gelin-S revealed two distinct thermal degradation events. These occurred at temperatures of 165 °C for Gelin-S and 241 °C for PAMA₂₁. Notably, the DSC curve also underwent noticeable modifications upon the introduction of Gelin-S. Two sharp, new endothermic peaks observed at 65 °C and 80 °C, attributed to the increased mobility of amorphous regions of Gelin-S [37]. Moreover, the enthalpy changes also reduced to -101 J/g and -3.7 J/g due to the incorporation of a greater amorphous phase from Gelin-S and the disruption of crystallinity stemming from the thiol-ene reaction.

Previous studies have along these lines demonstrated that Pantoan polymers form helical structures along their backbone due to hydrogen interactions between adjacent hydroxyl groups on its backbone. These changes in thermal behavior are most likely linked to the rupture of hydrogen bonds between adjacent pantoan polymers after methacrylation and incorporation of Gelin-S, which in turn reduce the crystallinity. Overall, the chemical characterizations confirm a successful methacrylation of pantoan and a successful formation of crosslinked hydrogel with Gelin-s. In the following section we will characterize the morphological and mechanical properties of the resulting hydrogel to highlight some of its advantageous properties from a muscle tissue engineering point of view.

2.2. Rheology and 3D printing

Here, we have characterized PAMA hydrogels containing different degrees of methacrylation in terms of their mechanical, rheological, and physio-morphological traits. Unfortunately, highly substituted methacrylate PAMA (PAMA₃₇) manifested poor hydrogel formation. Because of this, we continued further studies with PAMA₂₁. To this end, we synthesized and compared three hydrogels with 2%, 3%, and 4% (w/v) of PAMA₂₁. The cross-sectional morphology of the hydrogels was characterized using a scanning electron microscope (SEM) [38] - all confirming that the hydrogels contained microporous structures with pore sizes in the range 10000–30000 μm² (Fig. 2 a). We did not observe any particular differences in morphology and pore size among the various tested combinations. Such high pore sizes are suitable for efficient exchange of nutrients and waste for optimal cellular metabolic activities (Fig. 2 b) [39,40]. From degradation studies we also observed a correlation between polymer concentration and degradability. The highest concentration (4% (w/v) of PAMA₂₁) displayed the highest stability with less than 10% mass loss after 14 days and the lowest swelling ratio (Fig. 2 c&d), whereas 2% displayed up to 60% mass loss after 14 days and the highest swelling ratio.

Injectable hydrogels hold great promise for stem cell therapies due to their ability to be used with minimal patient discomfort and a low risk of infection. Considering this, we conducted a thorough investigation into the rheological properties of our PAMA₂₁ combinations to assess their suitability in this context. Fig. 2e illustrates that the storage modulus (G') and loss modulus (G'') of the solutions increased as the concentration of PAMA₂₁ increased. Up to oscillation stress levels of around 1 Pa, both G' and G'' remained constant, with G' being larger than G'' for all concentrations. Within this region the viscoelastic materials remain in an unperturbed state, until a crossover occurs, after which the materials are identified as permanently perturbed. This behavior is likely influenced by electrostatic interactions between hydroxyl and methacrylate groups, as well as hydrogen bonding between nearby hydroxyl groups. However, at higher stress levels above 1 Pa, both G' and G'' decrease significantly, crossing over. This indicates a transition to a more liquid-like phase, where the pre-polymer solutions begin to flow. This phenomenon, known as shear-thinning behavior, implies that the solutions have a solid-like state, transitioning to a liquid-like state during shear, and returning to a solid state post-injection. Interestingly, all solutions exhibited a significant decrease in viscosity of approximately 10-fold within the range of 20 Pa s to around 1 Pa s when subjected to shear rates between 0.1 and 100 s⁻¹. Notably, this shear rate range aligns with the shear rates typically employed during the needle injection (27 G - 28 G needle) phase by surgeons (100-1000 s⁻¹) and in 3D extrusion bioprinting. For sake of comparison, very liquid-like solutions such as castor oil, glycerin and corn syrup display viscosities around 0.9–1.2 pas. In summary, the rheological analysis of the pre-polymer solutions supports the extrusion of PAMA₂₁ through small-diameter needles, making it suitable for injection-based stem cell therapies or 3D printing of hydrogels.

The shear-thinning properties of the developed materials prompted us to conduct a series of 3D printing experiments to evaluate their potential as bio inks. By leveraging the unique rheological behavior of these materials, we aimed to explore their suitability for fabricating complex structures with high precision and biocompatibility. We did this by analyzing the shape fidelity, printability ratio and spreading ratio of the printed constructs (Fig. 2f–h). We specifically focused on 2% and 4% PAMA₂₁ solutions. To this end, shape fidelity refers to how accurately the printed object matches the digital CAD model, whereas printability represents the ratio of successful prints to the total number of attempted prints and the spreading ratio measures the degree to which a 3D printed material or ink spreads on the printing substrate during the printing process. All together, these metrics can give insights into the overall quality, performance, and reliability of the 3D printing process, helping to optimize parameters for better results in future

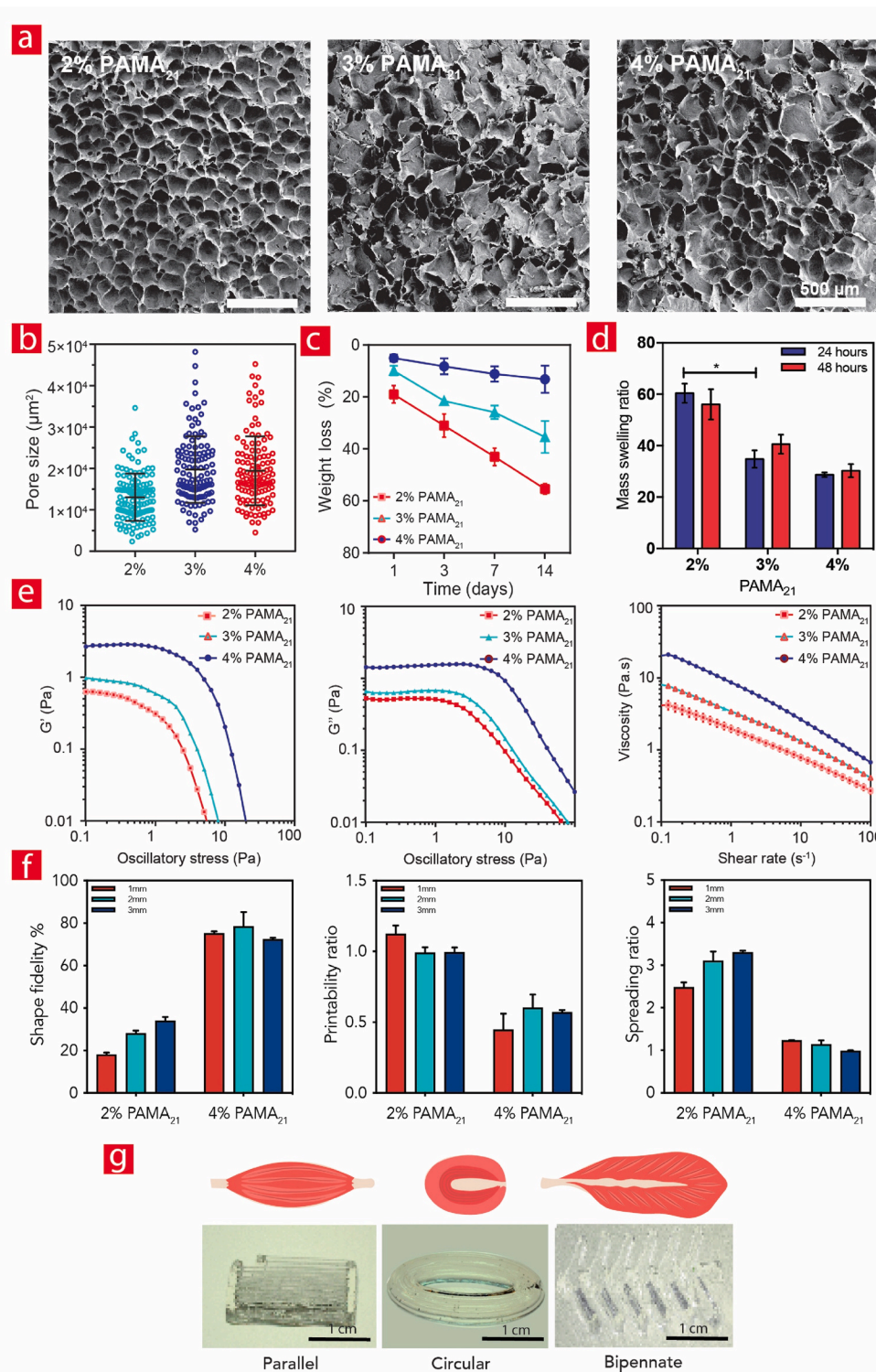


Fig. 2. Morphological, stability assays and rheological properties. (a) Scanning electron microscopy (SEM) of the 2, 3 and 4% PAMA₂₁ hydrogel variants developed herein. (b) Pore sizes within the imaged hydrogels were analyzed with ImageJ and are displayed. (c) Weight loss and (d) swelling profile of PAMA₂₁ hydrogels with different concentration (2, 3 and 4%). (e) The rheological properties (storage modulus (G'), loss modulus (G'') and Viscosity) of PAMA₂₁ (2, 3, and 4% w/v). (f) Quantification of the printability of PAMA₂₁ hydrogels. (g) Snapshots of the printed PAMA scaffolds like the native shapes of various muscles.

applications. From Fig. 2f we notice a really low shape fidelity below 40% for the 2% PAMA₂₁ inks, something that increases to around 80% for the 4% inks. This trend is reversed in terms of printability ratios, as this number is substantially higher for the 2% inks – this could be due to the fact that even though the shape fidelity is better for the 4%, they are more difficult to extrude due to their higher viscosity. Regarding the

spreading we can conclude that the 2% inks spread a lot, whereas the 4% inks maintained a good ratio around 1. Overall, these results indicate that while the post-prints are much better for the 4%, they are a bit more difficult to print due to their more solid-like state compared to the 2% ones. The good printability of the 4% inks prompted us to print more complicated constructs that we denoted parallel, circular and bipennate

with good fidelity (Fig. 2g).

2.3. Mechanical properties

In addition to their microstructural and rheological properties, the mechanical characteristics of hydrogels also play a crucial role in supporting native-like cellular functions. This is particularly significant in the context of skeletal muscle tissue engineering, as the mechanical environment can directly impact the cell efficacy and therapeutic outcomes. Skeletal muscle tissues are inherently dynamic and exhibit varying mechanical properties under different physical and biological conditions. The modulus values of skeletal muscle tissues typically fall within the range of 10–100 kPa [41]. Therefore, understanding and replicating the mechanical properties of native skeletal muscle tissues is crucial for the success of muscle tissue engineering and regeneration approaches. By recapitulating these mechanical cues in hydrogel-based scaffolds, engineers can tailor an environment that can support the

growth, differentiation, and maturation of muscle cells, ultimately leading to the development of functional and contractile muscle tissue substitutes. For these reasons, the mechanical properties of the hydrogels were tested in compression mode. From here, we evaluated their compression modulus, stress, energy dissipation, and recovery after five consecutive cycles of loading and unloading (Fig. 3a–b). Initially, we conducted tests on pristine PAMA₂₁ hydrogels without Gelin-S incorporation. These samples demonstrated impressive compressibility, with the ability to withstand up to 70% strain for five cycles (Fig. 3b). The recovery percentage was consistently high, ranging between 94% and 96% (Fig. 3c). As the polymer content increased, the mechanical properties of the hydrogels improved significantly. Higher polymer content resulted in a several-fold increase in stress at the 70% strain point compared to hydrogels with 2% PAMA₂₁, albeit with higher dissipation in the 3% and 4% PAMA₂₁ hydrogels (Fig. 3d). In more detail (Fig. 3e), hydrogels prepared with 4% PAMA₂₁ exhibited the highest ultimate stress (94.8 ± 9 kPa) and modulus (4.7 ± 0.7 kPa), while the 2%

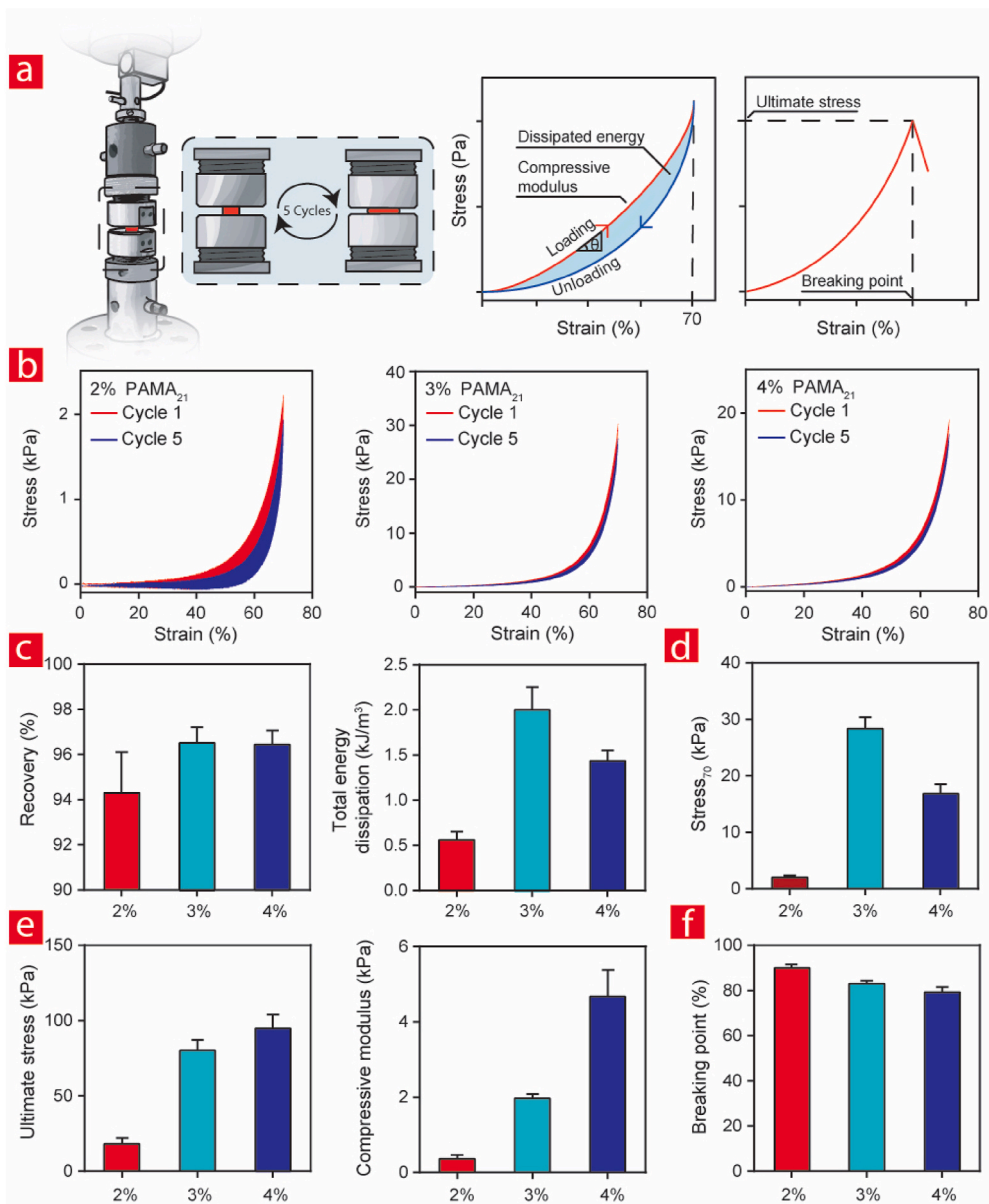


Fig. 3. Mechanical analysis. (a) Brief explanation of the working principle behind the mechanical analysis of hydrogels. (b) Cyclic stress–strain curves (up to five cycles) corresponding to 2, 3 and 4 % PAMA₂₁ hydrogels cross-linked in the presence of 0.5% photoinitiator. (c) Mechanical recovery and total energy dissipated after 70% strain were retrieved from the stress–strain curves. (d) Stress at 70% strain for 2, 3 and 4 % PAMA₂₁ hydrogels. (e) Ultimate stress and compressive modulus of the respective hydrogels as shown here. (f) Strain at breaking point of the respective hydrogels.

hydrogels were considerably softer, with the lowest ultimate stress (18 ± 4 kPa) and modulus (0.4 ± 0.1 kPa) values. Remarkably, the 2% hydrogels showed breaking points at around 90% compressive strain, surpassing other reported compressible hydrogels reported in the field. On the other hand, the 3% and 4% hydrogels had breaking points around 80% (Fig. 3f). We therefore decided to only focus on 2% PAMA₂₁ and decided to refer to this as simply PAMA₂₁ for the sake of clarity. After the incorporation of Gelin-S, PAMA₂₁ hydrogels maintained their exceptional compressibility, still breaking at around 75% compressive strain. However, the recovery rate slightly decreased to 90% at 60% strain. On the other hand, the compressive modulus increased from 0.4 kPa to 15 kPa and therefore fell within the range of native skeletal muscle tissues (Supplementary Fig. 2). The compressive modulus also fell within the range of native skeletal muscle tissues, approximately 15 kPa (Supplementary Fig. 2). Overall, the mechanical studies demonstrate that pristine PAMA hydrogels hold promise for skeletal muscle tissue engineering applications from a dynamic perspective, as they exhibit high compressibility, good cyclability, and efficient recovery. Nevertheless, the stiffness remained suboptimal and below the range of native-like muscle tissues. This limitation was effectively addressed through the inclusion of Gelin-S, without significantly compromising the resilience and durability of the hydrogel systems.

2.4. Cell viability

Cell viability plays a critical role in the development of scaffolds for

tissue engineering applications. While previous studies have investigated the viability of various polysaccharides such as Alginate, Hyaluronic Acid, Chitosan, and Carrageenan, demonstrating promising outcomes, it is important to note that the biocompatibility of our newly synthesized PAMA has not been extensively explored. Since PAMA has been produced for the first time in our laboratory, it necessitates extra attention in terms of its biocompatibility. It is therefore crucial to conduct thorough assessments and investigations to examine how cells interact and respond to the presence of pantoan. We therefore evaluated the viability of C2C12 encapsulated in PAMA₂₁ using a Live/Dead staining kit at different time points up to two weeks of culture (Fig. 4). As shown in Fig. 4b and quantified in Fig. 4c–d, representative images taken at different time points proved that PAMA₂₁ provides suitable compatibility toward the encapsulated cells after UV exposure. It has been shown in Fig. 4e that even after two weeks of in-vitro culture, the cells encapsulated in PAMA₂₁ had a viability of 69%. In order to increase PAMA₂₁ support toward the encapsulated cells, Gelin-S as a cell-adhesive protein-based biopolymer was added to this system [30]. This formulation change maintained the cell viability at around 80% and induced C2C12 cells to spread within the composite hydrogel (Supplementary Fig. 2). All in all, these results proved that the developed system could sufficiently support encapsulated muscle cells both in terms of their viability and spreading capacity and thus ready for down-stream biological assays.

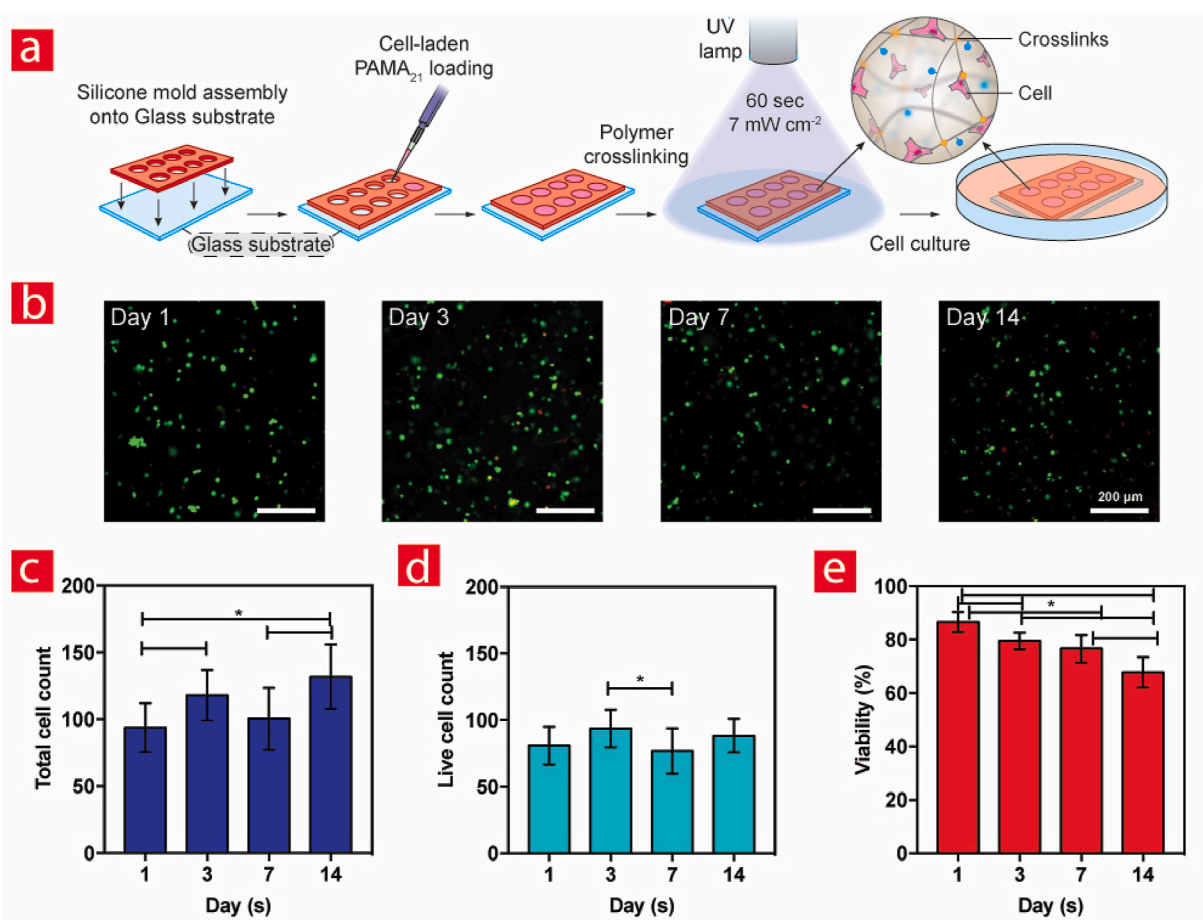


Fig. 4. C2C12 viability evaluation after encapsulating in PEMA₂₁ UV crosslinked hydrogels. (a) Schematic showing the steps behind the mold preparation, C2C12 encapsulation, crosslinking, and culture. (b) Representative images of cells encapsulated in PEMA₂₁ after being stained with calcein-AM (green, live cells) and ethidium homodimer-1 (red, dead cells) at different time points. (c) Number of total and (d) Live cells observed in cell-laden hydrogels at different time points. (e) C2C12 viability after 1, 3, 7, and 14 days in culture.

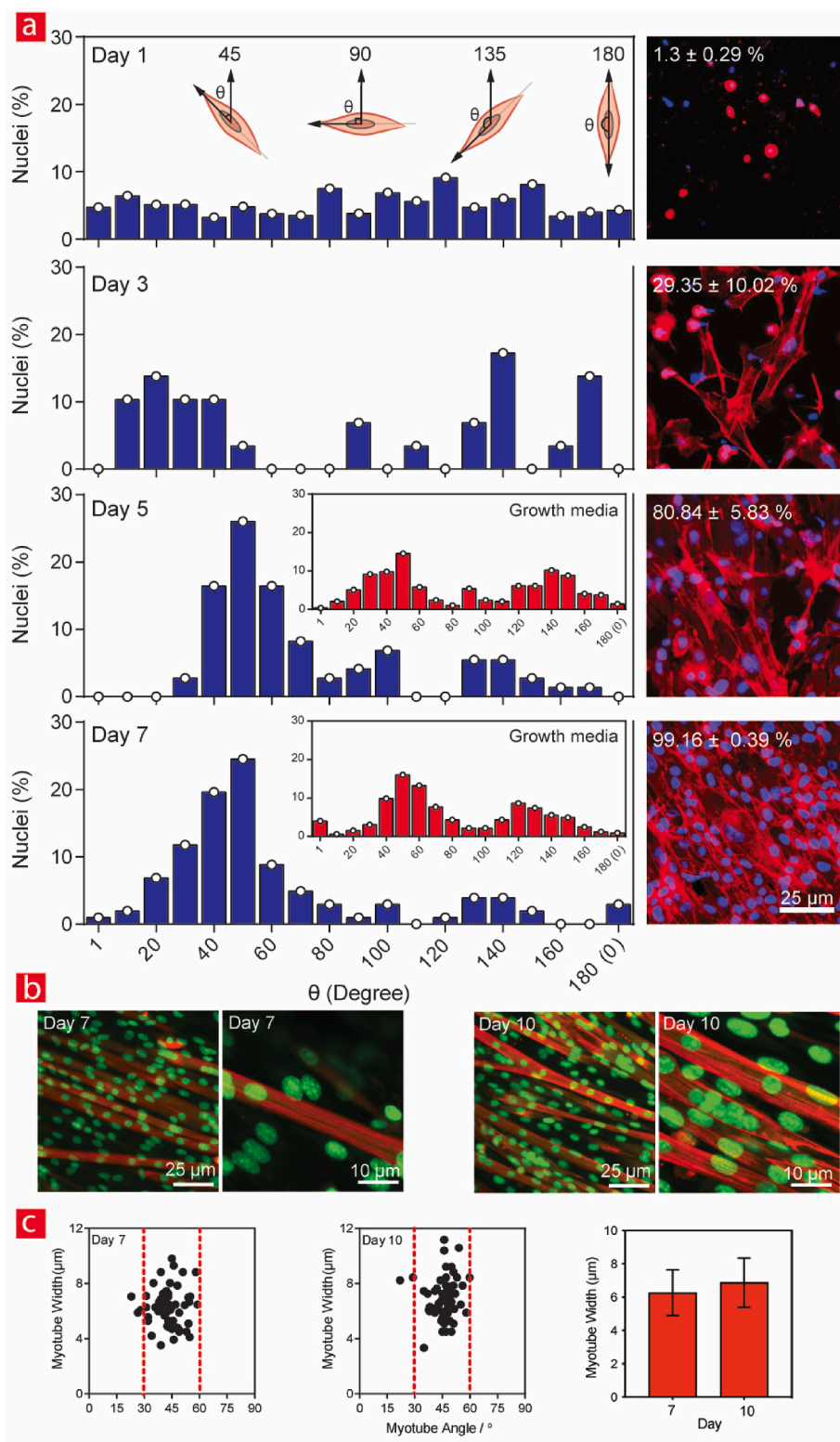


Fig. 5. (a) C2C12 spreading and alignment visualized by fluorescent staining (phalloidin/Hoechst) and confocal microscopy at different time points (1, 3, 5, and 7 days) and different types of media. The fluorescent images show F-actin (red) and nucleus (blue) for the cells encapsulated in PEMA₂₁-Gelin-S hydrogels. The first two graphs and their associated images are related to the samples conditioned in growth media. The two bottom images are taken on day 5 and 7 from the samples conditioned in the differentiation media. The percentages shown on the images are an estimation of cellular confluency inside the hydrogels. (b) Fluorescent images of alpha-actinin (in red) immunostained cells encapsulated in PEMA₂₁-Gelin-S hydrogels after 7 and 10 days of culture in differentiation media. (c) Alignment analysis of the immunostained cells in (b).

2.5. C2C12 alignment and myotube formation

One crucial aspect that requires thorough investigation during the development of a biomaterial for skeletal muscle tissue engineering is the alignment and differentiation of myoblasts. This specific parameter has been carefully assessed and measured in the context of C2C12 cells encapsulated in PAMA₂₁-Gelin-S hydrogels (Fig. 5a). This evaluation plays a vital role in understanding the behavior and functionality of PAMA in supporting a native-like growth and maturation of skeletal muscle tissue. Indeed, by quantifying the myoblast alignment and differentiation within the hydrogel system, we can gain valuable insights into how effectively the biomaterial promotes the desired cellular responses necessary for successful muscle tissue engineering.

On day 1 and 3 (in the cell growth phase), we did not observe cell alignment, as evidenced by the random alignment of myoblasts in the hydrogels (Fig. 5a). After day 5, while the fluorescence images of the samples in growth media showed a bimodal distribution of the orientation angles, the cells cultured in differentiation showed a clearer unidirectional alignment (Fig. 5a). Moreover, the analysis of images taken at different time points revealed that PAMA provided a suitable microenvironment for C2C12 proliferation and spreading through alignment as their confluency reached about 99% in only one week regardless of the media type used (data not shown). Since myoblast multiplication is one of the essential phases of myogenesis [42], this observation also demonstrated that PAMA₂₁-Gelin-S is a promising biomaterial for muscle tissue engineering.

Immunostaining was performed to examine the cell-laden PAMA₂₁-Gelin-S hydrogels that were incubated in differentiation media for 7 and 10 days. The objective was to accurately confirm the differentiation of the C2C12 into mature myotubes within the developed system. As depicted in Fig. 5 b, the immunofluorescence staining demonstrated that the PAMA₂₁ composites could provide a suitable microenvironment within which the encapsulated myoblasts could fuse into myotubes

expressing a pivotal protein that define muscle sarcomeres (alpha-actinin). Notably, myotubes were striated and multinucleated, which are important characteristics of the native milieu during skeletal muscle regeneration. By analyzing the images in more depth, we detected slightly higher myotube width and more uniformly aligned myotubes on day 10 compared to day 7, albeit the difference was not significant.

2.6. In vivo results

To explore the potential of photo-crosslinked PAMA₂₁ and PAMA₂₁-Gelin-s hydrogels for *in vivo* skeletal muscle regeneration, we designed a study using a rat model of VML (Volumetric Muscle Loss) in the Tibialis Anterior (TA) muscle. The experimental procedure involved injecting PAMA₂₁ and PAMA₂₁-Gelin-s-based hydrogels into the site of the muscle defect, as depicted in Fig. 6a–c. To assess the progress of the skeletal muscle regeneration, histological examinations were conducted at various time points, specifically 7 and 21 days post VML. These examinations involved carefully analyzing tissue samples to gain insights into the cellular and structural changes occurring within the regenerated muscle (Fig. 6d). Such histological examinations offer valuable information about the extent of muscle regeneration, cellular organization, revascularization, and potential integration of the hydrogel within the tissue. By analyzing the sequential changes in the histological features over time, we can obtain a better understanding of the efficacy and therapeutic potential of our hydrogels in promoting successful skeletal muscle regeneration.

As shown by the representative macroscopic tissue images of the leg, there was skeletal muscle regeneration without signs of infection, fluid accumulation under the skin (seroma) and visible scarring after injecting PAMA₂₁-Gelin-s in the lacerated regions after seven days post-injury (Fig. 6a–c). In stark contrast to the hydrogel treatment groups, there was a much more prominent “gap” in the non-treatment group at the defect site (Fig. 6a–c). In fact, in the non-treatment groups, the TA

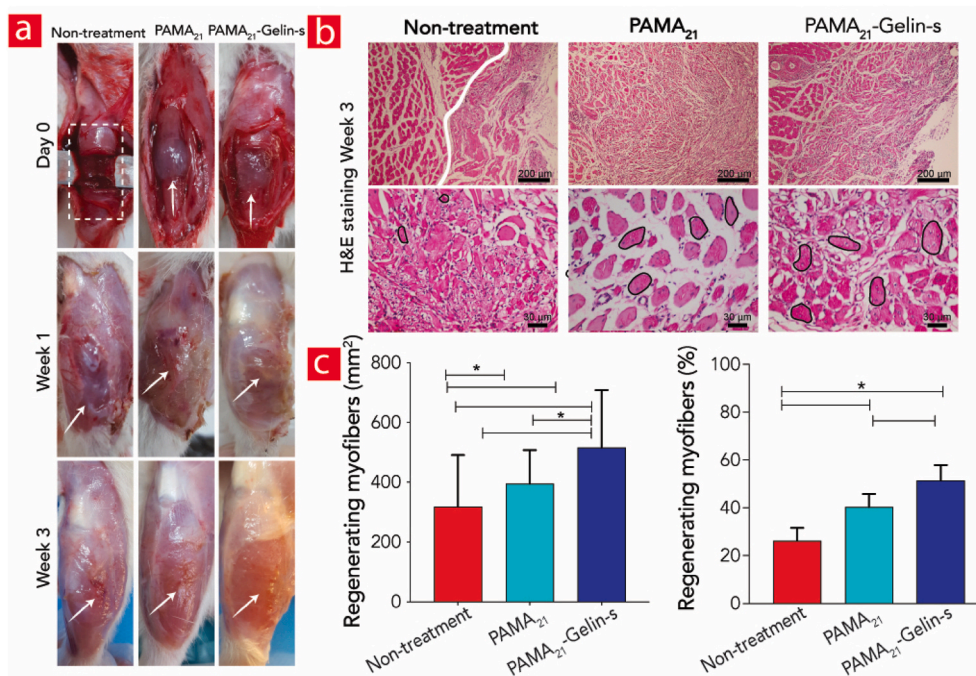


Fig. 6. Histological comparison of the Tibialis Anterior (TA) volumetric muscle loss (VML) injury site before and after and hydrogel implant treatment. (a) Photograph of the surgical site of the defect site after 7 and 21 days post-injury. The white lines denote defect site boundaries, and white arrows illustrate treatment location within the different times post VML surgery. VML injury was created by an excision of approximately (8 mm diameter × 3 mm deep) of the TA muscle. Immediately after defect creation, the fascia layer was sutured, and PAMA and PAMA-Gelin-s hydrogels were injected through the incision, in the area between fascia and muscle, the skin was closed, and the animal was allowed to recover (not shown). (b) H&E staining of the histological slides after 3 weeks. (c) Quantitative analysis of regenerating myofibers (%), and mean area of regenerating myofibers (μm²) at 21 days post-injury. Columns with star superscripts between one another are significantly different from one another ($p < 0.05$).

muscle was virtually indistinguishable from the uninjured counterpart, especially after seven days post-injury (Fig. 6b). Although PAMA hydrogel implantation did not promote robust functional recovery, significant volume reconstitution was still apparent in this group. Of particular importance is the observation that new muscle tissue formation was observed after 21 days post-injury (Fig. 6). Indeed, there were more newly formed muscle tissue and significant volume recovery in both PAMA₂₁ and PAMA₂₁-Gelin-s compared to non-treatment groups. However, some regenerated tissues appeared in the non-treated animals as well (Fig. 6c), even though the defects were still evident 21 days post-VML operation.

The Hematoxylin-Eosin (H&E) histochemical staining was employed

to evaluate skeletal muscle regeneration within the examined hydrogels (Fig. 6d). In the H&E stain, the nuclei are stained with a blue-purple color, and cellular proteins are stained with a red pink (Fig. 6d). Specifically, myofiber regeneration was quantitatively analyzed at 21 days post-injury for the different injured areas and assessed by the percentage of centrally-located nuclei as a sign of regenerating myofibers (Fig. 6e). It was found that all the hydrogel-treated groups showed an increased number of myofibers displaying centrally located nuclei (newborn myofibers) when compared to the non-treated groups (Fig. 6e) with PAMA₂₁-Gelin-S showing the highest amount. Indeed, PAMA₂₁-Gelin-s (51.4 ± 6.3%) showed significantly higher numbers of centrally located nuclei myofibers after 21 days post-injury than the non-treated groups

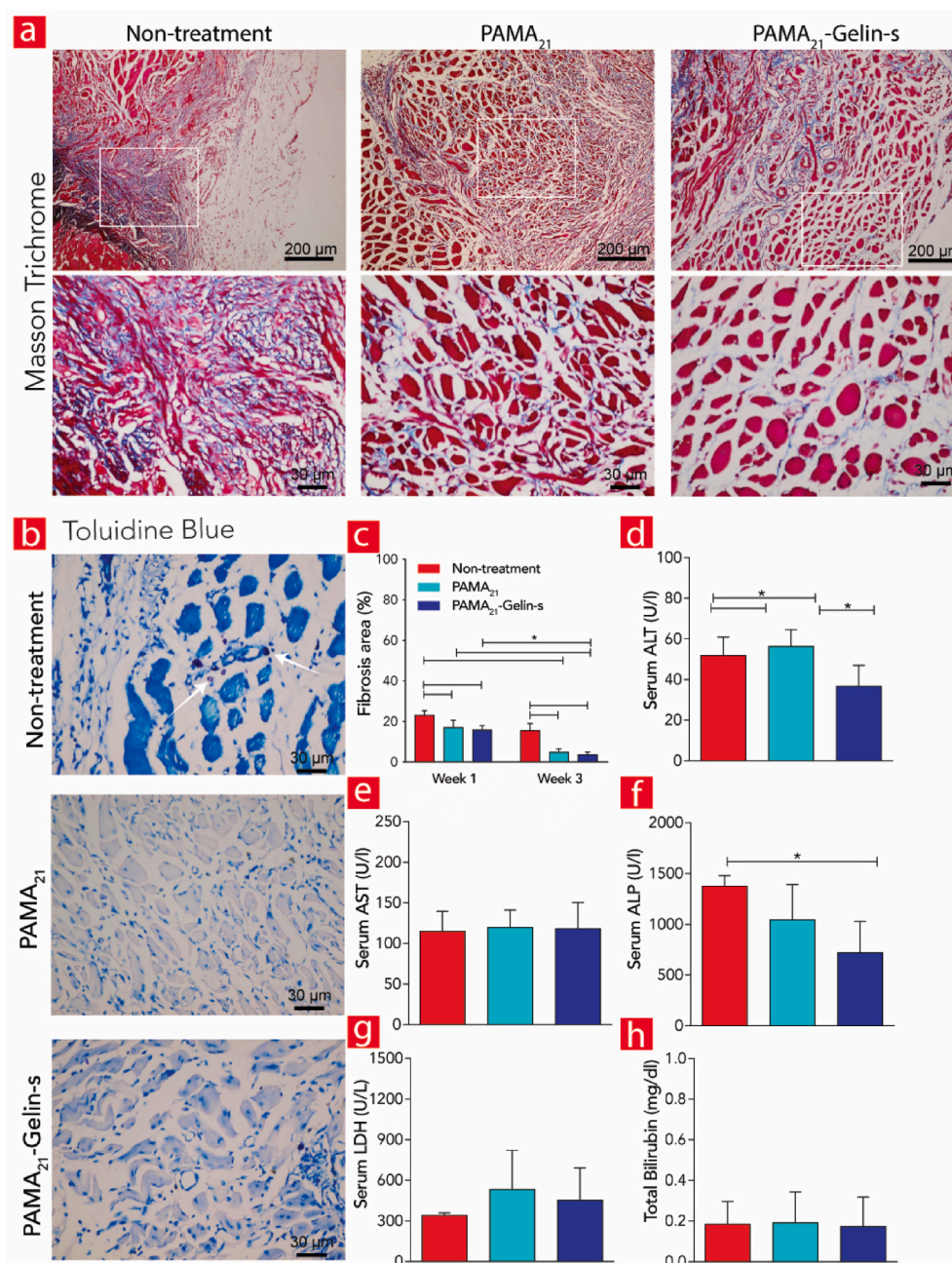


Fig. 7. Toluidine Blue and Masson's Trichrome Histological comparison and Blood serum analysis at 21 days post-injury. (a) Histological comparison by Toluidine Blue -stained sections of tissue retrieved from the implant region of injured TA muscle at 21 days post-injury. (b) Histological comparison by Masson's Trichrome -stained sections of tissue retrieved from implant region of injured TA muscle at 21 days post-injury and Quantification analysis of fibrosis area (%). (c) Blood serum biochemical parameters at 21 days post-injury. Columns with star superscripts between one another are significantly different from one another ($p < 0.05$).

(25.9 ± 5.9) and pristine PAMA-hydrogel treated animals (39.9 ± 5.3) (Fig. 6e). In general, a quantitative analysis of the relative cross-sectional area of TA muscle for all three groups at 21 days post-injury showed that PAMA₂₁-Gelin-s and PAMA₂₁ samples had significantly higher retention cross-sectional area than non-treatment samples (Fig. 6e). The higher retention rate is most likely linked with the incorporation of Gelin-s, since it contains the arginine-glycine-aspartic acid (RGD) sequence, which is essential for facilitating myoblast attachment with the surrounding EMC to direct myoblast cell proliferation and differentiation [43]. These results confirmed that PAMA₂₁-Gelin-s could efficiently enhance the regeneration of skeletal muscle tissue with a much better regenerative capacity than the non-treatment VML group and PAMA₂₁ alone.

Masson Trichrome staining was used to evaluate cellular morphology as well as the presence of fibrotic areas (collagen deposition) (Fig. 6a). While there was some evidence of residual fibrosis and inflammatory infiltrates after seven days post-injury (Supplementary Fig. 4c), there was also significantly less fibrosis at both time points for PAMA₂₁-Gelin-s hydrogels than the pristine group. Meanwhile, the hydrogel-treated groups seemed to positively inhibit the formation of disordered collagen fibers as compared with the non-treatment group following 21 days after the surgical procedure. We also investigated the biocompatibility of our PAMA-based hydrogel by looking into possible unwanted inflammatory responses in a post-implantation scenario via a toluidine blue staining (Fig. 7a). To this end, we discovered mast cells with irregularities and fissures in the muscle surface of the non-treatment group, while the hydrogel treatment groups instead exhibited homogeneous staining (Fig. 7b). Our focus here was on Mast cells accumulation and subsequent activity in the injury site, as Mast cells are widely acknowledged for their roles in inflammation and allergic reactions [44,45]. Finally, the total fibrosis area was also measured after seven days post-injury (Fig. 7c), amounting to 23.2% for non-treated, 17.1% for PAMA₂₁, and 15.9% for PAMA₂₁-Gelin-s treated animals. After 21 days post-injury, this trend did not change much for non-treated animals dropping to 15.6 % only, whereas it dropped substantially for PAMA₂₁ and PAMA₂₁-Gelin-s treated animals at 4.8% and 3.6 %, respectively.

Finally, we turned to a blood serum analysis to determine whether the function of vital organs such as liver and kidney could be damaged due to possible toxic byproducts associated with the hydrogel degradation process. Liver function markers including alanine aminotransferase (ALT), aspartate aminotransferase (AST), alkaline phosphatase (ALP), lactate dehydrogenase (LDH) and total bilirubin were assessed (Fig. 7d–h). ALP, AST, and total bilirubin are used as a marker for the detection of bile duct obstruction, cellular injury in the liver. Therefore, potential damaging foreign materials can alter the concentration of these markers in serum [46–48]. Fig. 7d–h shows not statistically significant ($p > 0.05$) differences between AST, ALP, and LDH serum biochemical parameters of control and hydrogel-treated groups after 21 days. In addition, no statistically significant difference was observed in the activity of total bilirubin between the normal and hydrogels-treated groups ($p > 0.05$). However, after 21 days, the serum ALT level was higher in the non-treatment and PAMA-treated groups compared to PAMA-Gelin-S groups, and there was a significant difference between serum ALP of non-treatment and PAMA-Gelin-S groups. All these data indicate that our hydrogel product is biodegradable but not toxic while simultaneously enabling the growth of new muscle tissue within its perimeters.

3. Discussion

The traumatic or surgical loss of skeletal muscle volume is a severe clinical complication that is characterized by fibrotic tissue deposition, lack of re-innervation, and insufficient muscle regeneration to bridge the defect site [14,49–54]. In order to effectively restore muscle regeneration and function in the injured site, a great variety of muscle tissue

engineering approaches has been surveyed in recent years [49–54]. Skeletal tissue engineering goes as far back as the early 1960's, when Konigsberg used chicken embryonic stem cells to generate cross-striated muscle fibers. Already then it was quite clear that collagen was critical in the development of mature muscle constructs. Other biopolymers including alginate, fibrin, gelatin and polycaprolactone (PCL)-based polymers have over the years emerged as viable options as well. From these studies it appears that the most promising solution in this regard is the use of injectable hydrogels with high bioactivity and cell-infiltration capacity. Firstly, their injectability allows for easy application and precise delivery to the affected site, enabling them to fill irregularly shaped defects. This is particularly beneficial for addressing volumetric muscle loss, where conventional methods may struggle to restore irregular loss of muscle volume. Secondly, the high bioactivity combined with superior cell permeability enables the implants to utilize the body's own reservoir of cells to accelerate the regeneration process.

A great variety of biomimetic hydrogel pre-polymers resembling those from the human extracellular matrix (ECM) have been used to create porous and cell-friendly 3D microenvironments for progenitor muscle cells to grow and thrive within. These including naturally occurring polymers such as alginate [55–57], keratin [52,58], collagen [59–61], gelatin [62–65], and fibrin [66–69] and hyaluronic acid. Especially, polysaccharides such as alginate have received great attention over the years due to their good bioactivities, natural abundance, biodegradability, biocompatibility, and chemical modifiability [30, 70–72]. They are typically crosslinked via metallic cations (Ca^{2+} , Mg^{2+} , Na^+ , K^+) due to their charged backbone [73–78]. Unfortunately, this methodology presents several disadvantages such as cation leakage or exchange, toxicity for cells, suboptimal mechanical properties, making them unsuitable as regenerative biomaterials [30,73,79]. Notably, systems based on alginate and other polysaccharides out there, are not sufficiently bioactive, not loadbearing and typically break around 50 % strain values. They are therefore not optimal for muscle tissue engineering. Indeed, it is quite difficult to endow multiple functionalities such as bioactivity, injectability, durability and native-like stiffness into biomaterial systems without unwanted tradeoffs or using complicated and potentially toxic chemical procedures. Obtaining strong mechanical properties and toughness in hydrogels is particularly challenging. This difficulty arises from the fact that hydrogels typically consist of up to 99% water. However, researchers have dedicated a whole sub-field to explore the development of mechanically robust hydrogels with maintained bioactivity, without damaging their water retention properties. This compromise is crucial as efficient nutrient, oxygen, and waste exchange with the surrounding environment heavily rely on the water retention capabilities of hydrogels.

Herein, we have turned to a novel approach based on an EPS from *Pantoea* sp. BCCS 001 GH bacteria known as Pantoan. Generally speaking, bacterial EPS's such as cellulose, xanthan, levan, gellan-based hydrogels have already been applied for a number of tissue engineering applications [38,71,73,75,80–82]. They have indeed become highly sought out in the field due to their varied chemical and material properties, as they can become produced in mass at a very low-cost, while displaying unique viscoelastic and wettability suitable for hydrogel-based stem cell niches and advanced bioinks. Importantly, they are easy to customize through genetically engineering of the microbial population. In recent years material engineers have capitalized upon these benefits to deliver a wide range of innovative materials. One of the key advantages with the Pantoan species is its high EPS production yields and good scalability. Even still, the application of this EPS in tissue engineering is still not fully explored, which makes this work quite unique compared to what's already out there. We have therefore in this study tried to utilize Pantoan in tissue engineering by transforming it into a UV-cross-linkable hydrogel with tunable mechanical properties, unprecedented high durability, and stability both *in vitro* and *in vivo* environments. For instance, we have shown that pantoan methacrylate (PAMA) can become fine-tuned to cover a broad range of ultimate

stresses ranging from 18 kPa to 95 kPa and young modulus ranging from 1 kPa–29 kPa and compressive strains close to 70 %. Importantly, we could obtain a high mechanical recovery of ~94, 96, and 96 % after five cyclic compressions at 90 % strain. To make the system even more bioactive we have incorporated Gelin-S into the system via a Michaelis reaction between thiol groups on gelatin and acrylate groups on PAMA. Specifically in this study we focused on developing a PAMA₂₁-Gelin-S hydrogels that offer both appropriate biophysical and cell-material cues to support optimal myogenic cell function and facilitate de novo skeletal muscle regeneration. Indeed, our results showed compressive modulus around 12.97 ± 4.2 kPa (Supplementary Fig. 3), which is near the ECM of healthy skeletal muscle average (12 ± 4 kPa). This is quite advantageous from the point-of-view of tissue regeneration since optimal myoblast differentiation occurs when seeded on substrates with tissue-like stiffness [83]. Indeed, it has been well documented that the mechanical properties of scaffolds play an important role in myoblast behavior [22]. For instance, in a groundbreaking study conducted by Adam Engler and colleagues, they demonstrated that the differentiation of mesenchymal stem cells is influenced by the stiffness of the substrate they are cultured on. Specifically, they found that when the substrate stiffness was 8–17 kPa, mesenchymal stem cells were more likely to differentiate into muscle cells. This discovery highlights the importance of substrate stiffness in directing lineage specificity during stem cell differentiation [84].

Super compressible hydrogels, like the one presented here, are typically created using synthetic methods [85]. These methods often utilize polyacrylamide [86–89], poly vinyl alcohol [90–92], or polyacrylic acid derivatives [93] as the main ingredients. However, acrylamide itself is highly toxic, and many of the components used in preparing poly vinyl alcohol or polyacrylic acid hydrogels such as tannic acid or carbon nanotubes can display toxicity. Additionally, these methods can be quite complex, and they lack bioactivity, making them less suitable for tissue engineering applications. On the other hand, alternative methods employing natural polymers like GelMA [94,95], silk fibroin [96], or elastin [97] have been successful in achieving high compressibility, typically ranging between 70% and 90%. For example, Laponite-reinforced GelMA hydrogels can withstand compressive strains of up to 90% before breaking, silk hydrogel crosslinking with horseradish peroxidase can reach up to 70%, and photocrosslinked elastin peptides can reach up to 70% as well. In our study, we were able to achieve 90% compression before breakage and super elastic behavior up to 70% strain by simply methacrylating an EPS and crosslinking it using UV-light. To the best of our knowledge, such remarkable super compressibility of natural hydrogel systems has never been achieved before through such a simple and scalable method. We believe that the remarkable super elasticity of the Pantoan molecule is attributed to its intrinsic conformational structure, which consists of helix formations formed by hydrogen bonding between its hydroxyl groups according to a previous study [29], and supported by our DSC and TGA results. Higher order conformational structure are not only observed in Pantoan but also in other polysaccharides, thanks to specific supramolecular forces in their solid state [98,99]. Similarly, in a significant study from 1970, it was discovered that the conformational state of a polymer has a greater impact on its elastic modulus and extensibility compared to the side groups [100]. This phenomenon can be seen in other biopolymers as well such as various polysaccharides and silk fibroin, where the energy required to unfold coil-like structures bonded by intermolecular forces is higher, and the recoiling of these structures due to reversible bonds can sometimes increase the overall durability [101]. It is reasonable to assume that a similar mechanism governs the impressive elasticity observed in the pristine PAMA systems. However, what sets this developed system apart is not only its remarkable super compressibility and high elasticity but also its compatibility for 3D bioprinting.

Porosity, pore architecture, swelling ratio, and degradation rate are other important properties defining cell fate and tissue regeneration. In this respect, PAMA₂₁ reached a swelling equilibrium in just 24 h with a

mass swelling ratio of 38 ± 4 which proves PAMA₂₁ porous structure. This in turn also enables an efficient exchange of water-soluble metabolites. PAMA is thus in theory thereby capable of maintaining high cell viability [15]. Indeed, the cell survival rate and the ability of cells to migrate, spread, differentiate, and connect with other cells are also imperative in tissue regeneration [102]. Our results showed that PAMA₂₁ could be used for 3D encapsulation of C2C12 cells with high viability and homogeneous 3D cell distribution, but due to the polysaccharide nature of pristine PAMA₂₁ it could not on its own facilitate sufficient cell–matrix interactions, and the cells barely spread. Like in the native ECM we added hydrolyzed collagen in the form of gelatin to also capture the cell-anchoring aspects of the natural ECM. To this end, we observed highly aligned cellular architectures which are of critical importance for skeletal muscle, and heart [103]. Indeed, during skeletal muscle tissue development, myoblasts' cytoplasm fuse after their alignment, forming a multinucleated fiber named myotube [42]. It has also been reported that more cell alignment improves cell fusion during myoblast differentiation [104]. A contributing factor in this direction could be the structural resemblance between EPS and natural glycans already present in muscle tissue. Indeed, several studies have shown that cells contain carbohydrate-binding domains capable of binding to glycans also present on EPS. Studies have also shown that glycans can participate as co-receptors during growth factor signaling involving TGF- β and EGF pathways [14,105]. This, together with the cell attachment and proliferation promoting capacities of gelatin, may be a key factor behind the cell spreading and alignment observed within the hydrogels. This feature is mainly attributed to the RGD peptide sequence present in Gelin-S, as this peptide has been reported to control myoblast adherence and phenotype [106,107].

To investigate whether this new system was applicable for healing muscle defects we used photo-crosslinked PAMA₂₁ and PAMA₂₁-Gelin-S hydrogel in a VML rodent model. Interestingly enhanced muscle regeneration in PAMA₂₁ and PAMA₂₁-Gelin-S treatment groups were observed throughout the 3-week course of study when compared with not-treated animals with the regeneration being slightly higher at around 45 % for PAMA₂₁-Gelin-S compared to 40 % for PAMA₂₁ (Fig. 6). In general, results confirmed that both PAMA₂₁ and PAMA₂₁-Gelin-S could efficiently enhance skeletal muscle tissue regeneration with a much better regenerative effect than the non-treatment VML group. Moreover, as shown in Fig. 6e both hydrogels resulted in volume reconstitution as well as myogenesis. These observations clearly highlight the efficacy of PAMA₂₁ as a potentially important platform for treating VML injury. In addition, the hydrogels were associated with significantly increased new tissue formation, including an abundance of new myofibers, presented as smaller diameter fibers with centrally located nuclei identified in surgical regions. To this end, myofibers with nuclei in the center of the cytoplasm are usually considered newborn myofibers, while the mature ones have nuclei on the periphery [108–110]. The results of Masson's trichrome staining indicated that the presence of hydrogel could effectively promote muscle remodeling and reduce tissue fibrosis and scarring from >20 % to <10 %. Overall, our results demonstrate that hydrogel treatment can heal muscle tissue defects to a substantial degree – specifically, we found that PAMA₂₁-Gelin-S resulted in the fastest and optimal recovery in this direction. This is likely linked with the incorporation of gelatin modified (Gelin-S) since it contains the arginine-glycine-aspartic acid (RGD) sequence, which is essential for facilitating myoblast attachment with the surrounding EMC to direct myoblast cell proliferation and differentiation – a pivotal step toward muscle tissue regeneration *in situ* [43].

There have been numerous studies showcasing the potential of hydrogels in enhancing muscle cell behavior and promoting healing in both *in vitro* and *in vivo* settings. However, many of these studies have utilized scaffolds made from brittle and weak materials such as muscle autografts [111], gelatin [62], fibrin [112,113], or decellularized extracellular matrices (ECMs) [49,114]. Others have employed chemically modified scaffolds based on thiolated hyaluronic acid [14] or

methacrylic acid [5], as well as synthetic counterparts like polycaprolactone [15]. While these studies have indeed reported exciting results in the field of muscle tissue engineering, many of these systems have exhibited either overly soft or excessively brittle characteristics. Moreover, those that displayed greater mechanical strength failed to possess the essential loadbearing properties necessary for a system of this nature. Furthermore, none of these systems exhibited the same level of compressibility and elasticity as the hydrogel introduced in our research, setting it apart from previous approaches. Notably, the system described here is based on readily available fermentation biomaterials that undergo a simple one-step chemical modification process (methacrylation). As a result, the hydrogel production process is easily scalable and can be manufactured at a significantly lower cost compared to other hydrogels currently available in the market. Notably, the PAMA₂₁-Gelin-s system offers a highly stable, mechanically durable, and tissue regenerative hydrogel without any unwanted compromises, even when using a low concentration (3%) of the material. For comparison, GelMA-based hydrogels, which are among the most commercially available, typically require higher concentrations, mostly exceeding 7% [64,115]. This higher concentration significantly increases the cost of the solution when compared to the one presented here. It is worth mentioning that many conventional hydrogels, apart from alginate, are also expensive due to complex multi-step production procedures.

We believe that the field of living materials for tissue engineering will experience significant growth in the coming decades and will benefit from mechanically robust, scalable, bioactive and most importantly bacteria-derived hydrogels. In a nutshell bacteria-derived materials can be designed to sense regenerative signals in stem cell-embedded scaffolds and respond with the release of growth factors or drugs [21–23,25,26]. They could also facilitate spontaneous healing in the event of material failure. To achieve optimal stem cell performance and prevent premature failure, it is crucial to utilize EPS derived from bacteria, like the one developed and described here. These EPS can create a self-sustaining environment for microbial populations and allow for the diffusion of nutrients and waste products in and out of the scaffold. This work therefore represents an important step towards the unexplored realm of regenerative machine biology. Another avenue, in which this work could become an important steppingstone is cell-based meat production. Indeed, replacing animals as a food source offers several societal benefits, including improved animal welfare, environmental advantages, and a more affordable source of essential proteins [116–118]. However, it is important to note that the current challenges in this field differ significantly from the optimistic claims made in the media. To fully realize the potential of manufacturing meat from skeletal muscle stem cells, further processing is required to capture essential nutrients and address texture and mechanical properties. Cell encapsulation and growth within native like 3D matrices with muscle like stiffness have greatly advanced matters along these lines. However, even more advances are within the reach by implementing sophisticated mechanical 3D stimulation – something which requires super elastic 3D matrices capable of undergoing repeated cyclic stimulation without breaking. The PAMA developed in this study not only exhibits mechanical properties resembling those of muscle tissue but also demonstrates durability that surpasses conventional matrices based on fibrin and collagen in the field and could therefore become a key player here.

4. Conclusion

Overall, the findings obtained from our study strongly suggest that the bioactive hydrogel system developed herein can efficiently guide myoblast behavior and facilitate their transition into functional muscle fibers holds great promise for therapeutic applications such as muscle repair, regeneration, and the development of in vitro models for drug screening and disease modeling. Furthermore, the relatively short period of time required for observing these positive effects is an encouraging factor, as it suggests the potential for even more efficient

and accelerated muscle tissue engineering strategies. Looking forward, the synthesis route used for obtaining PAMA was scalable, and low-cost with the polymer itself being non-toxic and biocompatible. For this reason, the gap into the biomedical industry is small. Using a biopolymer from bacteria also opens for a new and almost futuristic opportunities within the emerging field of living materials. Such distinctive living attributes can be used in implants with theragnostic properties, sophisticated biosensors, smart drug delivery systems, living wearables, materials for smart buildings, or as self-growing materials for building sustainable extraterrestrial habitats.

5. Materials and methods

5.1. Materials

Methacrylic anhydride (94%), 2-hydroxy-4'-(2-hydroxyethoxy)-2-methylpropiofenone (Irgacure 2959), deuterium oxide (D₂O, 99.9% in D), bovine serum albumin (BSA), β-glycerophosphate disodium salt hydrate, Dulbecco's phosphate-buffered saline (DPBS), Dulbecco's modified Eagle's medium (DMEM)-high glucose, antibiotics (penicillin/streptomycin), trypsin–ethylene diamine tetraacetic acid (EDTA) solution 1x, Triton X-100, formaldehyde, Isopropyl alcohol, and dialysis tubing cellulose membrane (14.0 k molecular weight cut-off) were obtained from Sigma-Aldrich (St. Louis, MO). Thiol-modified gelatin (Gelin-S) and degassed deionized water (DG water) at pH 5.0–8.0 were supplied by ESI-BIO (Alameda, CA, USA). C2C12 cell line (ATCC CRL-1772) was purchased from LGC Standards, Sweden. Fetal bovine serum (FBS) and fetal horse serum (FHS) were obtained from Biowest, France. Ketamine 10 % and Xylazine 2% were obtained from Alfasan CO., Netherlands. Rhodamine phalloidin and Hoechst 33342 were purchased from Thermo Fisher Scientific (Waltham, MA). Thiopental was purchased from Loghman Pharmaceutical & Hygienic Co., Iran. Silicone Isolators (JTR24R-1 and C18142) were purchased from Grace Bio-Labs (Oregon, USA) and Molecular Probes (Leiden, The Netherlands), respectively. Paraformaldehyde (16% w/v aqueous solution) was obtained from Electron Microscopy Sciences (Hatfield, PA, USA). Mouse monoclonal anti-α-actinin (sarcomeric) antibody (A7732) and goat anti-mouse IgG H&L (Alexa Fluor® 555) (ab150114) were purchased from Sigma-Aldrich and Abcam.

5.2. Production, extraction, and purification of pantoan

Pantoan exopolysaccharide, composed of repeating disaccharide units of glucose and galactose, was naturally produced under controlled conditions by fermentation of a plant pathogenic bacteria, *Pantoea* sp. BCCS 001 GH, isolated from nectarine fruit. *Pantoea* sp. BCCS 001 GH under the specific accession number of “SUB3753631 *Pantoea* MH026116”, was acquired from the culture collection of the Pharmaceutical Sciences Research Centre, Shiraz University of Medical Sciences, Iran. This strain was maintained at –80 °C in yeast extract-peptone and dextrose (YPD) medium (2% dextrose, 1% yeast extract and 2% peptone) containing 25% (v/v) glycerol. The bacteria were cultured in yeast extract-peptone and dextrose (YPD) medium in a shaker incubator for 24 h at 30 °C and 200 rpm. The media contained (g/L) sucrose (30 g/L), KH₂PO₄ (3 g/L), MgSO₄ (0.2 g/L), (NH₄)₂SO₄ (2 g/L), citric acid (2 g/L), H₃BO₃, (6 mg/L), ZnCl₂ (6 mg/L), FeCl₃ (2.4 mg/L), and CaCl₂ (20 mg/L). After preparation, the media acidity was adjusted to 7 and then autoclaved at 121 °C for 20 min. The fermentation process was cultivated under aerobic conditions for 48 h, using a YPD inoculum volume of 2% (v/v) as previously described [29]. After 48 h of cultivation, the cells were separated by high-speed centrifugation for 20 min at 11,000 rpm and 25 °C. The cell-free supernatant containing Pantoan was autoclaved for 30 min at 100 °C to deactivate bacterial enzymes and thereby prevent polymer degradation [29]. Pantoan was precipitated by adding water miscible non-solvents alcohol (isopropanol) with a ratio (isopropanol to water 4:1 v/v) of alcohols to a culture broth at 4 °C.

Afterwards, the precipitated pantoan was dissolved in deionized water (28 h, 25 °C) and then dialyzed through a cellulose membrane (14.0 k molecular weight cut-off) for three days to remove all debris and remaining reagent. Finally, the resulting solution of purified pantoan was lyophilized by a freeze drier, and pantoan powder was kept in a freezer at –20 °C.

5.3. Synthesis of pantoan methacrylate (PAMA)

In brief, 1 g of pantoan powder was dissolved in 100 ml Milli-Q water at room temperature by stirring. For pantoan methacrylation in a low and high degree, 1.5 ml and or 2.5 ml of methacrylic anhydride was added to the solution, respectively. The solution acidity was adjusted 8.5 by adding sodium hydroxide (5 M). This reaction continued for 24 h at room temperature in the dark under a fume hood. The resulting mixture was dialyzed against distilled water using the 14.0 kDa cut-off dialysis tubing for one week at room temperature to remove the impurities and unreacted reagents. The final mixture was lyophilized to obtain PAMA.

5.4. Preparation of prepolymer solution of PAMA-gelin-S

Gelin-S powder was dissolved in DG water at 37 °C for 3 h through vortex to reach 1.5% (w/v) solution. Subsequently, lyophilized PAMA with 21% methacrylation degree (PAMA₂₁) and the photoinitiator (Irgacure 2959) were added to the Gelin-S solution so that their final concentrations were fixed at 1.5% (w/v) and 0.5% (w/v), respectively. It was gently vortexed for 20 min to obtain a homogenous mixture. The mixture was kept in a 37 °C incubator until the photocrosslinking step.

5.5. Preparation of photocrosslinked hydrogels

To prepare PAMA-based hydrogels, 2, 3, and 4% (w/v) PAMA₂₁ were dissolved in a photoinitiator [52] solution of 0.5% (w/v) in DPBS at room temperature through stirring for 3 h. Afterwards, 100 µl of PAMA₂₁ polymer solutions was deposited between a poly(methyl methacrylate) slide and a glass coverslip separated by a 2 mm spacer. The samples were exposed to ultraviolet [119] light (365 nm) ~7 mW/cm² for 60 s to form PAMA-based hydrogels. The same procedure was applied to a mixture of PAMA₂₁ and Gelin-S with the final concentration of 1.5% w/v for both to prepare PAMA₂₁-Gelin-S hydrogels. After photocrosslinking, the samples were washed four times with warm DPBS to remove unreacted materials.

5.6. Fourier transform infrared (FTIR) spectroscopic characterization

FTIR spectroscopy was employed to observe functional groups (hydroxyl and methacrylate) before and after the methacrylation step using a PerkinElmer Spectrum 100 FTIR spectrometer (USA) equipped with an attenuated total reflection (ATR) accessory. The transmittance spectra of lyophilized PAMA₂₁, PAMA₃₇, and PAMA₂₁-Gelin-S samples (N = 3 for each group) were recorded at 25 °C over the range of 4000 - 500 cm⁻¹ at a resolution of 4 cm⁻¹ for 16 scans and analyzed following the background subtraction.

5.7. Proton nuclear magnetic resonance (¹H NMR) characterization of PAMA₂₁

The methacryloyl modification of PAMA was confirmed by performing ¹H NMR spectroscopy. The pantoan purified powder, PAMA₂₁, and PAMA₃₇ (2% w/v) were prepared in D₂O separately and transferred to NMR tubes for ¹H NMR spectroscopy. The ¹H NMR spectra were recorded using a Varian Mercury 400 MHz spectrometer (USA) at 25 °C under the spectral width of 8012.82 Hz, the acquisition time of 8.18 s, and 6.5 ms pulses. For these recordings, tetramethylsilane (TMS) was used as the internal standard. The chemical shifts (δ) were obtained in parts per million (ppm) related to the solvent signal peak. In order to

estimate the methacrylation degree, the relative integrated intensities of methyl protons peak at ~1.9 ppm present in the methacrylated samples were compared with H-4 signal at ~4.4 ppm in the pantoan molecule.

5.8. Zeta potential analysis

Zeta potential of pantoan, PAMA₂₁, and PAMA₃₇ prepolymer solutions (0.01% w/v in Milli-Q water) were measured at room temperature by laser Doppler anemometry using a Malvern Zetasizer instrument (Nano Series ZS, Malvern Instruments, Worcestershire, U.K.), which was equipped with a 4 mW He–Ne laser, operating at a wavelength of 632.8 nm.

5.9. Thermal properties

The thermal properties of pantoan, and PAMA₂₁ were characterized using a TA TGA Q500 Thermogravimetric analyzer (USA), a TA DSC Q200 differential scanning calorimeter (DSC, USA). Thermogravimetric analysis (TGA) was carried out inside a nitrogen-saturated furnace; all the while, the furnace temperature was increased linearly with a rate of 10 °C min⁻¹ from 20 to 800 °C, and monitored the mass loss as function of temperature under a constant nitrogen flow at 60 mL min⁻¹. Furthermore, the differential scanning calorimetric (DSC) analysis was conducted by increasing the chamber temperature linearly from 25 to 280 °C with a heating rate of 10 °C min⁻¹. DSC was examined under a dynamic nitrogen flow (50 mL min⁻¹). To perform the DSC analysis, the pantoan, and PAMA₂₁ were encapsulated into Tzero aluminum pans (Switzerland), while an empty pan was used as a reference. The change in heat flow as a function of temperature was monitored, and the observed exothermic peak was interpreted as the crystallization temperature of the respective hydrogels.

5.10. Scanning electron microscopy

Hydrogels morphology and average pore size were characterized using SEM (FEI Quanta 200 ESEM FEG) in an accelerating voltage of 10 kV under a high vacuum. To this end, the photocrosslinked hydrogel samples (N = 3 for each group) were washed with double-distilled water, lyophilized, and cross-sectioned. Then, a 10 nm thick gold layer was sputter-coated on the samples before SEM imaging. Four images were randomly picked from the SEM images pool for each sample, and ImageJ software (National Institutes of Health (NIH)) was used to calculate the apparent pore size distribution.

5.11. Swelling and degradation studies

The effect of prepolymer concentration on the swelling behavior and stability of the photocrosslinked pantoan hydrogels was investigated by measuring hydration kinetics and dissolution behavior. Briefly, to assess the swelling behavior, two sets of PAMA₂₁ hydrogels were soaked in DPBS and then incubated at 37 °C for 24 and 48 h, to reach an equilibrium swelling state. At the respective time points, the swollen weight (W_s) of each sample was recorded after gently blotting the excess DPBS with a Kimwipes paper from the hydrogel surface. Then, the swollen hydrogels were freeze-dried to record their dry weight (W_d). At least three replicates were performed for each combination. The swelling ratio was then calculated from the following equation [120]:

$$\text{Swelling ratio} = \frac{W_s - W_d}{W_d} \quad (1)$$

To evaluate the hydrogel degradation rate, at least three hydrogels per combination were prepared for every time point (1, 3, 7, and 21 days). They were first freeze-dried, and their initial weights were recorded (W_i). Then, these samples were incubated in 1 ml DPBS at 37 °C for the mentioned time points. At every time point, the dry weights (W_f) of the respected samples were recorded after freeze-drying. The

degradation rate was calculated using equation (2).

$$\text{Mass loss (\%)} = \left(\frac{W_f}{W_i} \times 100 \right) - 100 \quad (2)$$

5.12. Rheological study

The rheological properties (loss modulus (G'') and storage modulus (G') of PAMA₂₁ (2, 3, and 4% w/v) were assessed at 25 °C using a Discovery Hybrid Rheometer HR-2 (TA Instrument, New Castle, United States) equipped with a 40 mm parallel plate geometry. To this end, the solutions were shortly agitated and subsequently pipetted on the rheometer. To determine the linear viscoelastic region (LVR), an amplitude sweep test was performed from 0.1 to 100 Pa at an angular frequency of 0.1 rad/s. In addition, steady shear experiments were performed at 25 °C to evaluate the effect of Pantoan and PAMA₂₁ pregel concentration on shear thinning behavior. In this regard, flow sweep experiments with a shear rate ranging from 0.1 to 100 s⁻¹ were conducted while the gap size was adjusted to 300 μm. All measurements were performed in triplicate.

5.13. 3D fabrication and bioprinting of PAMA₂₁ hydrogels

Different 3D structures mimicking the architecture of native muscles were fabricated using an extrusion-based 3D printing system (3D Discovery, regenHu, Switzerland). Initially, PAMA was dissolved in MQ water with two different concentrations of 2 wt% and 4 wt% (2PAMA and 4PAMA). Afterwards, the hydrogels were transferred to a 5 mL syringe (Nordson EFD, USA) and extruded through a 27G conical nozzle, 0.2 mm (Nordson EFD, USA) at 10 °C. Continuous hydrogel deposition was achieved by applying a dispensing pressure of 0.5 bar. To evaluate the printability of the hydrogel, 2PAMA and 4PAMA were printed with the shape of crosshatch 90/0, with different interfiber spacing of 1 mm, 2 mm and 3 mm. Briefly, three scaffolds with one layer of filaments were printed, and images were acquired with a stereomicroscope (Leica) immediately after the printing. Their diameter and length were calculated using ImageJ software (National Institutes of Health). The shape fidelity, printability ratio, and the spreading ratio was calculated based on following equations:

$$\text{Shape fidelity} = \frac{A_t - A_s}{A_t} \times 100$$

$$\text{Spreading ratio} = \frac{\text{Printed needle diameter}}{\text{Needle diameter}}$$

$$\text{Printability ratio} = \frac{\pi}{4} \times \frac{1}{C}$$

Where, A_t and A_s are the theoretical and experimental surface of the pores and C is the circularity of an enclosed area ($C = \frac{4\pi A}{L^2}$), L stands for perimeter and A for area.

5.14. Mechanical properties of PAMA₂₁ and PAMA₂₁-gelin-s hydrogels

The mechanical properties of hydrogels were carried out using an Instron (Model 5967, UK) mechanical tester equipped with a 50 N load cell. Compressive and cyclic compression tests were accomplished by applying a strain rate of 0.5 mm min⁻¹ and strain levels up to about 90%. The cylindrical photocrosslinked hydrogels (~10 mm diameter, ~2 mm height, $N = 6$) were prepared. The prepared hydrogels were first incubated in DPBS overnight at 37 °C. Then, prior to mechanical tests, excess liquid from the samples was removed using Kimwipes paper, and the diameter and height of the hydrogels were measured using a digital Vernier caliper. The compressive modulus of the samples was determined by calculating the slope of the acquired stress-strain data between 20 and 30% strain. Afterwards, cyclic compression testing (loading and

unloading) was performed for five cycles, during which PAMA₂₁ and PAMA₂₁-Gelin-s samples were compressed at the rate of 0.5 mm min⁻¹ for up to 70 and 60% strain, respectively. The recovery (%) was obtained by dividing the toughness (area under the stress-strain curve) of the second and first recovery cycles. The total dissipated energy during the five cycles was calculated based on the area between the loading and unloading hysteresis curves, using OriginPro 2017 software (Northampton, MA, USA). Six replicates were used for each hydrogel composition and test.

5.15. C2C12 cell culture and 3D encapsulation

Murine C2C12 myoblasts were cultured in a humidified incubator at 37 °C in a 5% CO₂ atmosphere. DMEM (high glucose) supplemented with 10% (v/v) FBS and 1% (v/v) penicillin/streptomycin was used as growth medium. The cells were harvested from T-75 flasks (Thermo Scientific™) at 60% confluency by trypsinization using 0.25% (w/v) trypsin and 0.02% (w/v) EDTA after rinsing twice with warm DPBS, and used for either subculture or experiments. The cells were used at passages 3 to 5 for live/dead assay and differentiation experiments. For 3D cell encapsulation in PAMA₂₁-Gelin-S, a solution of 1.5 ml containing 30 mg PAMA₂₁, 30 mg Gelin-S, and 10 mg of Irgacure 2959 were prepared as the prepolymer solution. Then, 500 μl of C2C12 cell suspension (8 × 10⁶ cells/ml) was gently mixed with the hydrogel precursor. The pregel containing C2C12 cells was deposited into microwell arrays with different sizes based on the experiment type. For the viability assay and immunostaining, the silicone isolator previously fixed on a glass slide, was used that could contain 10 μl pregel in each microwell (2 mm diameter x 1 mm depth). For cell alignment assessment, 100 μl of pregel was deposited in another type of microwell (9 mm diameter x 2.5 mm depth). Finally, the cell-laden hydrogels were obtained through UV light-assisted crosslinking. Following five times wash with DPBS, the samples were cultured in growth media. When the cell confluency in the hydrogels reached 60–70%, the growth media was replaced by the differentiation media consisting of DMEM (high glucose) supplemented with 2% v/v horse serum and 1% (v/v) penicillin/streptomycin. Cell confluence was estimated based on the percentage of the surface area of two-dimensional (2D) hydrogel that was covered with cells. During the culture and differentiation period, media was refreshed every other day.

5.16. Viability assay

To assess the viabilities of the encapsulated cells at different time points (1, 3, 7 and 14 days of culture), a viability kit (LIVE/DEAD™ Viability/Cytotoxicity Kit, Thermo Fisher Scientific, USA) was employed according to the manufacturer's instructions. Briefly, the hydrogels were washed two times with warm DPBS and then covered in a solution of 4 μM calcein-AM and 10 μM ethidium homodimer-1 in DPBS for 15 min in the dark. The samples were washed with DPBS to remove the excess fluorescent dyes and then examined using a confocal laser scanning microscope (Zeiss LSM 700, Germany). Using ImageJ (National Institutes of Health, USA), the obtained images were split into green and red channels to count live and dead cells, respectively. Finally, cell viability was calculated by dividing the live cell count by the total number of cells in each image. Six samples were assessed for each experimental condition and time point, and at least three images were analyzed for each sample.

5.17. Cell spreading and Cellular Alignment

The spreading and alignment of C2C12 cells in the PAMA₂₁-Gelin-S hydrogels were evaluated via fluorescent staining. The experimental group consisted of encapsulated cells cultured in growth medium for three days after which they were cultured in differentiation medium for further four days. The control group consisted of encapsulated cells that were cultured in growth medium for seven days. Samples for staining

were selected at days 1, 3, 5 and 7. Before the staining, the samples were washed three times with warm DPBS and then fixed in a solution of paraformaldehyde (4% w/v in DPBS) for 15 min at room temperature. The fixed samples were permeabilized by incubation in 0.1% (w/v) Triton X-100 diluted in DPBS at room temperature. A solution of 1% (w/v) BSA in DPBS was utilized to block the samples at room temperature for 30 min. Next, the samples were incubated in a solution of Rhodamine phalloidin (diluted 1:40 in 0.1% (w/v) BSA) for 45 min at 37 °C in the dark to perform the actin cytoskeleton staining. The hydrogels were finally washed three times in DPBS for 1 min, and then the nuclei of the cells were stained by incubation in Hoechst (diluted 1:2000 in DPBS) for 15 min at 37 °C in the dark. The samples were then washed three times in DPBS and imaged using confocal laser scanning microscopy (Zeiss LSM 700, Germany). Finally, the cell spreading and alignment were quantitatively evaluated using ImageJ. By assuming an elliptical shape for the cell nucleus, the degree of alignment was defined as the angle formed by the semi-major axis of an elliptical nucleus with a reference direction (vertical axis of the 2D reference frame). The reference direction coincides with an inertial direction in the lab frame. The analysis was performed on at least six specimens for each condition.

5.18. Immunostaining of cell-laden hydrogels

At the respected time point (7 and 10 days in differentiation media), the PAMA₂₁-Gelin-S hydrogels were washed with DPBS three times and fixed in 4% (w/v) paraformaldehyde for 15 min at room temperature. Then, the samples were washed with DPBS three times to remove paraformaldehyde and permeabilized with 0.3% (w/v) Triton X-100 in DPBS for 15 min at room temperature. The samples were washed extensively in DPBS, and further blocked using 2% (w/v) BSA for 30 min to circumvent any unspecific binding of the antibodies. Samples were then incubated for 2 h at 37° in a solution of primary antibody alpha-actinin (diluted 1:200 in 1% (w/v) BSA), and then washed three times with DPBS. The samples were incubated for 1 h at room temperature with a solution of the secondary antibody of goat anti-mouse IgG H&L conjugated to Alexa Fluor 555 (diluted 1:200 in 1% (w/v) BSA). Finally, the samples were washed three times in DPBS, and then incubated in Hoechst 33342 for 30 min at 37 °C to stain the nuclei of the cells. The samples were then rinsed three times in DPBS and observed using a confocal laser scanning microscope (Zeiss LSM 700, Germany). In both time (7 and 10 days) Myotube width was obtained by calculating at least 50 individual diameters of Myotube using image j. The angle was defined the same as Cellular Alignment part which was based on the nucleus direction.

5.19. Animal care and surgical procedure

Male Sprague Dawley rats (n = 42; 250–300 g weight) were obtained from the Laboratory Animals Breeding Center (Shiraz University of Medical Sciences, Shiraz, Iran). Animals were housed in plastic cages over woodchip bedding in a standard environment (23 ± 1 °C, 12:12 light: dark cycles, 40% relative humidity). During experiments, rats were allowed free access to tap water and a regular standard rodent's chow diet (Behparvar®, Tehran, Iran). All the experiments were performed in conformity with animal care and use protocols approved by an ethics committee in Shiraz University of Medical Sciences, Shiraz, Iran (#98-01-05-19528).

Rats underwent volumetric muscle loss (VML) injury based on previously established protocols [54,121]. Briefly, animals were first anesthetized with an intraperitoneal administration of ketamine 10% (100 mg/kg) and xylazine 2% (5 mg/kg). The surgical site (rat thigh muscles) was shaved and sterilized with ethanol before skin incision. The tibialis anterior (TA) muscle of the right leg was identified and separated bluntly from the underlying fascia covering the anterior compartment, and an injury (8 mm × 8 mm × 3 mm depth) was made on the muscle. Six animals per time point per condition were used for the

experimental groups of not treated VML and treated with PAMA₂₁ and or PAMA₂₁-Gelin-S hydrogels. For no treatment group, the injury was left without any intervention. In the treated groups, the respected hydrogels were deposited in the VML site, where they were crosslinked by UV light (365–395 nm) for 60 s using a UV flashlight (UV302D, Shenzhen Lightfe Lighting Co., China). Finally, the skin incision was sutured and then was cleaned with a betadine pad to prevent infection. Six rats without VML injury were considered as the control group.

5.20. Blood serum analysis and tissue histopathological alterations

At the predetermined time points (week one and three), the animals were deeply anesthetized with an IP administration of thiopental (100 mg/kg). Then, blood was collected from the abdominal aorta of each animal and transferred to standard tubes (Improvacuter®, Guangzhou, China), and centrifuged at 4 °C for 10 min at 4000 rpm to separate serum. The acquired sera were analyzed by an automated benchtop biochemistry analyzer (Mindray BS-200®, Guangzhou, China) and commercial kits provided by Pars Azmun® (Tehran, Iran) in order to assess serum alkaline phosphatase (ALP), alanine aminotransferase (ALT), lactate dehydrogenase (LDH), aspartate aminotransferase (AST), and total bilirubin (TB) content. After blood sampling, skin on the hind limb for each animal was removed to expose the injured site for gross imaging and morphology analysis. Then, the TA muscle was gently detached and removed for histological analysis. In this regard, the acquired TA muscle tissues were fixed overnight in 10% formalin buffer (0.4% w/v NaH₂PO₄, 0.64% w/v Na₂HPO₄, and 10% v/v formaldehyde in double-distilled water). Then, the fixed tissues were paraffin-embedded and sectioned to obtain 5 μm transverse sections for assessing tissue fibrosis, inflammation, and regeneration. For this purpose, the sections were stained with Mason's trichrome, hematoxylin and eosin (H&E), and toluidine blue. From the taken images using a light microscope (Olympus CX21®, Japan), parameters including the percentage of regenerating myofibers, mean cross-sectional area (CSA) of total myofibers, and fibrosis area were scored and quantitatively compared using ImageJ for different experimental groups [52]. Myofiber regeneration was quantitatively assessed three weeks post-injury by the percentage of newly regenerated myofibers (determined with centrally located nuclei) to the total myofibers observed in each slide. The CSA of the myofibers was assessed for the same images by measuring the area of total myofibers in each sample. Similarly, ImageJ was employed to quantify the different areas differentiated by Masson Trichrome staining and therefore evaluate the fibrosis in percentage after one and three weeks.

Ethics approval and consent to participate

All the experiments were performed in conformity with animal care and use protocols approved by an ethics committee in Shiraz University of Medical Sciences, Shiraz, Iran (#98-01-05-19528).

CRediT authorship contribution statement

Seyyed Vahid Niknezhad: Writing – review & editing, Writing – original draft, Methodology, Formal analysis, Data curation, Conceptualization. **Mehdi Mehrali:** Conceptualization, Data curation, Formal analysis, Methodology, Writing – original draft, Writing – review & editing. **Farinaz Riyahi Khorasgani:** Data curation, Formal analysis, Methodology, Writing – review & editing. **Reza Heidari:** Formal analysis, Project administration, Supervision, Writing – original draft, Writing – review & editing. **Firoz Babu Kadumudi:** Data curation, Formal analysis, Writing – original draft, Writing – review & editing. **Nasim Golafshan:** Writing – review & editing, Writing – original draft, Formal analysis, Data curation. **Miguel Castilho:** Writing – review & editing, Writing – original draft, Formal analysis, Data curation. **Cristian Pablo Pennisi:** Writing – review & editing, Writing – original draft, Supervision, Formal analysis. **Masoud Hasany:** Writing – review &

editing, Writing – original draft, Formal analysis, Data curation. **Mohammadjavad Jahanshahi:** Writing – review & editing, Formal analysis, Data curation. **Mohammad Mehrali:** Writing – review & editing, Writing – original draft, Formal analysis, Data curation. **Younes Ghasemi:** Writing – review & editing, Supervision, Formal analysis. **Negar Azarpira:** Writing – review & editing, Project administration, Formal analysis. **Thomas L. Andresen:** Writing – review & editing, Writing – original draft, Project administration. **Alireza Dolatshahi-Pirouz:** Writing – review & editing, Writing – original draft, Supervision, Project administration, Funding acquisition, Conceptualization.

Declaration of competing interest

The authors declare that they have no known competing financial interests or personal relationships that could have appeared to influence the work reported in this paper.

Acknowledgement

A.D.-P. would like to acknowledge the Danish Council for Independent Research (Technology and Production Sciences, 8105-00003B), Denmark; the Novo Nordisk Foundation (NNF22OC0079994 in the call "Project Grants in the Natural and Technical Sciences 2022), Denmark; and the VIDU research programme with project number R0004387, which is (partly) financed by The Netherlands Organization for Scientific Research (NWO), The Netherlands. This work has also received funding from the European Union's Horizon 2020 research and innovation programme under grant agreement no. 951747. Masoud Hasany and Mehdi Mehrali would like to acknowledge the European Union's Horizon 2020 research and innovation program under the Marie Skłodowska-Curie grant agreement No 899987.

Appendix A. Supplementary data

Supplementary data to this article can be found online at <https://doi.org/10.1016/j.bioactmat.2024.04.006>.

References

- [1] J.R. Sorensen, J. Mcfaline-Figueroa, J.A. Call, Pathophysiology of volumetric muscle loss and targets for regenerative rehabilitation, *Regenerative Rehabilitation: From Basic Science to the Clinic* (2022) 177–225. Springer.
- [2] K.H. Nakayama, M. Shayan, N.F. Huang, Engineering biomimetic materials for skeletal muscle repair and regeneration, *Adv. Healthcare Mater.* 8 (5) (2019) 1801168.
- [3] W.M. Han, S.E. Anderson, M. Mohiuddin, D. Barros, S.A. Nakhai, E. Shin, I. F. Amaral, A.P. Pêgo, A.J. García, Y.C. Jang, Synthetic matrix enhances transplanted satellite cell engraftment in dystrophic and aged skeletal muscle with comorbid trauma, *Sci. Adv.* 4 (8) (2018) eaar4008.
- [4] E. Mihaly, D.E. Altamirano, S. Tuffaha, W. Grayson, Engineering skeletal muscle: building complexity to achieve functionality, *Semin. Cell Dev. Biol.* (2021) 61–69. Elsevier.
- [5] M.M. Carleton, M.V. Sefton, Injectable and degradable methacrylic acid hydrogel alters macrophage response in skeletal muscle, *Biomaterials* 223 (2019) 119477.
- [6] A. Khademhosseini, R. Langer, A decade of progress in tissue engineering, *Nat. Protoc.* 11 (10) (2016) 1775–1781.
- [7] D. Sengupta, S.D. Waldman, S. Li, From in vitro to in situ tissue engineering, *Ann. Biomed. Eng.* 42 (7) (2014) 1537–1545.
- [8] I.K. Ko, S.J. Lee, A. Atala, J.J. Yoo, In situ tissue regeneration through host stem cell recruitment, *Exp. Mol. Med.* 45 (11) (2013) e57–e57.
- [9] E.M. Bueno, J. Glowacki, Cell-free and cell-based approaches for bone regeneration, *Nat. Rev. Rheumatol.* 5 (12) (2009) 685.
- [10] T. Jensen, T. Jakobsen, J. Baas, J.V. Nygaard, A. Dolatshahi-Pirouz, M. B. Hovgaard, M. Foss, C. Bunker, F. Besenbacher, K. Soballe, Hydroxyapatite nanoparticles in poly-D,L-lactic acid coatings on porous titanium implants conducts bone formation, *J. Biomed. Mater. Res.* 95a (3) (2010) 665–672.
- [11] T. Jensen, A. Dolatshahi-Pirouz, M. Foss, J. Baas, J. Lovmand, M. Duch, F. S. Pedersen, M. Kassem, C. Bunker, K. Soballe, F. Besenbacher, Interaction of human mesenchymal stem cells with osteopontin coated hydroxyapatite surfaces, *Colloids Surf., B* 75 (1) (2010) 186–193.
- [12] J.L. Drury, D.J. Mooney, Hydrogels for tissue engineering: scaffold design variables and applications, *Biomaterials* 24 (24) (2003) 4337–4351.
- [13] K.Y. Lee, D.J. Mooney, Hydrogels for tissue engineering, *Chem. Rev.* 101 (7) (2001) 1869–1880.
- [14] N. Narayanan, Z.H. Jia, K.H. Kim, L.J. Kuang, P. Lengemann, G. Shafer, V. Bernal-Crespo, S.H. Kuang, M. Deng, Biomimetic glycosaminoglycan-based scaffolds improve skeletal muscle regeneration in a Murine volumetric muscle loss model, *Bioact. Mater.* 6 (4) (2021) 1201–1213.
- [15] Y. Xu, X. Chen, Y. Qian, H. Tang, J. Song, X. Qu, B. Yue, W.E. Yuan, Melatonin-based and biomimetic scaffold as muscle-ECM implant for guiding myogenic differentiation of volumetric muscle loss, *Adv. Funct. Mater.* 30 (27) (2020) 2002378.
- [16] N. Annabi, A. Tamayol, J.A. Uquillas, M. Akbari, L.E. Bertassoni, C. Cha, G. Camci-Unal, M.R. Dokmeci, N.A. Peppas, A. Khademhosseini, 25th anniversary article: rational design and applications of hydrogels in regenerative medicine, *Adv. Mater.* 26 (1) (2014) 85–124.
- [17] S. Talebian, M. Mehrali, N. Taebnia, C.P. Pennisi, F.B. Kadumudi, J. Foroughi, M. Hasany, M. Nikkhah, M. Akbari, G. Orive, Self-healing hydrogels: the next paradigm shift in tissue engineering? *Adv. Sci.* 6 (16) (2019) 1801664.
- [18] M. Mehrali, A. Thakur, C.P. Pennisi, S. Talebian, A. Arpanaei, M. Nikkhah, A. Dolatshahi-Pirouz, Nanoreinforced hydrogels for tissue engineering: biomaterials that are compatible with load-bearing and electroactive tissues, *Adv. Mater.* 29 (8) (2017) 1603612.
- [19] H. Park, S.W. Kang, B.S. Kim, D.J. Mooney, K.Y. Lee, Shear-reversibly crosslinked alginate hydrogels for tissue engineering, *Macromol. Biosci.* 9 (9) (2009) 895–901.
- [20] M.F. Moradali, B.H.A. Rehm, Bacterial biopolymers: from pathogenesis to advanced materials, *Nat. Rev. Microbiol.* 18 (4) (2020) 195–210.
- [21] X.Y. Liu, H. Yuk, S.T. Lin, G.A. Parada, T.C. Tang, E. Tham, C. de la Fuente-Nunez, T.K. Lu, X.H. Zhao, 3D printing of living responsive materials and devices, *Adv. Mater.* 30 (4) (2018).
- [22] A.M. Duraj-Thatte, A. Manjula-Basavanna, J. Rutledge, J. Xia, S. Hassan, A. Sourlis, A.G. Rubio, A. Lesha, M. Zenkl, A. Kan, D.A. Weitz, Y.S. Zhang, N. S. Joshi, Programmable microbial ink for 3D printing of living materials produced from genetically engineered protein nanofibers, *Nat. Commun.* 12 (1) (2021).
- [23] A. Rodrigo-Navarro, S. Sankaran, M.J. Dalby, A. del Campo, M. Salmeron-Sanchez, Engineered living biomaterials, *Nat. Rev. Mater.* 6 (12) (2021) 1175–1190.
- [24] H. Chen, X. Zhang, Engineered bacteria-based living biomaterials for biomedical applications, *Front. Bioeng. Biotechnol.* 1 (2022) 22334.
- [25] J. Huang, S. Liu, C. Zhang, X. Wang, J. Pu, F. Ba, S. Xue, H. Ye, T. Zhao, K. Li, Programmable and printable *Bacillus subtilis* biofilms as engineered living materials, *Nat. Chem. Biol.* 15 (1) (2019) 34–41.
- [26] A.M. Duraj-Thatte, N.M.D. Courchesne, P. Praveschotinunt, J. Rutledge, Y. Lee, J. M. Karp, N.S. Joshi, Genetically programmable self-regenerating bacterial hydrogels, *Adv. Mater.* 31 (40) (2019) 1901826.
- [27] C. Gilbert, T.C. Tang, W. Ott, B.A. Dorr, W.M. Shaw, G.L. Sun, T.K. Lu, T. Ellis, Living materials with programmable functionalities grown from engineered microbial co-cultures, *Nat. Mater.* 20 (5) (2021) 691.
- [28] S.V. Niknezhad, M.H. Morowvat, G.N. Darzi, A. Irajy, Y. Ghasemi, Exopolysaccharide from *Pantoea* sp BCCS 001 GH isolated from nectarine fruit: production in submerged culture and preliminary physicochemical characterizations, *Food Sci. Biotechnol.* 27 (6) (2018) 1735–1746.
- [29] S.V. Niknezhad, G. Najafpour-Darzi, M.H. Morowvat, Y. Ghasemi, Exopolysaccharide production of *Pantoea* sp BCCS 001 GH: physical characterizations, emulsification, and antioxidant activities, *Int. J. Biol. Macromol.* 118 (2018) 1103–1111.
- [30] M. Mehrali, A. Thakur, F.B. Kadumudi, M.K. Pierchala, J.A.V. Cordova, M.-A. Shahbazi, M. Mehrali, C.P. Pennisi, G. Orive, A.K. Gaharwar, Pectin methacrylate (PEMA) and gelatin-based hydrogels for cell delivery: converting waste materials into biomaterials, *ACS Appl. Mater. Interfaces* 11 (13) (2019) 12283–12297.
- [31] G. Eke, N. Mangir, N. Hasirci, S. MacNeil, V. Hasirci, Development of a UV crosslinked biodegradable hydrogel containing adipose derived stem cells to promote vascularization for skin wounds and tissue engineering, *Biomaterials* 129 (2017) 188–198.
- [32] S. Laksee, S. Puthong, P. Kongkaviton, T. Palaga, N. Muangsin, Facile and green synthesis of pullulan derivative-stabilized Au nanoparticles as drug carriers for enhancing anticancer activity, *Carbohydr. Polym.* 198 (2018) 495–508.
- [33] T. Shen, S. Gnanakaran, The stability of cellulose: a statistical perspective from a coarse-grained model of hydrogen-bond networks, *Biophys. J.* 96 (8) (2009) 3032–3040.
- [34] R.P. Singh, M.K. Shukla, A. Mishra, P. Kumari, C. Reddy, B. Jha, Isolation and characterization of exopolysaccharides from seaweed associated bacteria *Bacillus licheniformis*, *Carbohydr. Polym.* 84 (3) (2011) 1019–1026.
- [35] P. Insulkar, S. Kerkar, S. Lele, Purification and structural-functional characterization of an exopolysaccharide from *Bacillus licheniformis* PASS26 with in-vitro antitumor and wound healing activities, *Int. J. Biol. Macromol.* 120 (2018) 1441–1450.
- [36] K. Shi, W. An, Q. Meng, Y. Gu, S. Liu, Partial characterization and lyoprotective activity of exopolysaccharide from *Onococcus oeni* 28A-1, *Process Biochem.* 101 (2021) 128–136.
- [37] R. Debone Piazza, J.V. Brandt, C. Carvalho dos Santos, R. Fernando Costa Marques, M. Jafelicci Junior, Gelatin/dextran-based hydrogel cross-linked by Diels-Alder click chemistry: the swelling and potassium diclofenac releasing, *Medical Devices & Sensors* 4 (1) (2021) e10151.
- [38] S. Unal, S. Arslan, B.K. Yilmaz, F.N. Oktar, A.Z. Sengil, O.J.C. Gunduz, Production and characterization of bacterial cellulose scaffold and its modification with hyaluronic acid and gelatin for glioblastoma cell culture 28 (1) (2021) 117–132.

- [39] N. Annabi, J.W. Nichol, X. Zhong, C.D. Ji, S. Koshy, A. Khademhosseini, F. Dehghani, Controlling the porosity and microarchitecture of hydrogels for tissue engineering, *Tissue Eng. Part B-Re* 16 (4) (2010) 371–383.
- [40] V. Karageorgiou, D. Kaplan, Porosity of 3D biomaterial scaffolds and osteogenesis, *Biomaterials* 26 (27) (2005) 5474–5491.
- [41] C.F. Guimarães, L. Gasperini, A.P. Marques, R.L. Reis, The stiffness of living tissues and its implications for tissue engineering, *Nat. Rev. Mater.* 5 (5) (2020) 351–370.
- [42] S.F. Gilbert, *Developmental Biology*, tenth ed., Sinauer Associates Inc, 2013.
- [43] B. Guo, J. Qu, X. Zhao, M. Zhang, Degradable conductive self-healing hydrogels based on dextran-graft-tetraaniline and N-carboxyethyl chitosan as injectable carriers for myoblast cell therapy and muscle regeneration, *Acta Biomater.* 84 (2019) 180–193.
- [44] S.K. Bortolotto, W.A. Morrison, X. Han, A. Messina, Mast cells play a pivotal role in ischaemia reperfusion injury to skeletal muscles, *Lab. Invest.* 84 (9) (2004) 1103–1111.
- [45] C.-P. Liao, R.C. Booker, J.-P. Brosseau, Z. Chen, J. Mo, E. Tchegnon, Y. Wang, D. W. Clapp, L.Q. Le, Contributions of inflammation and tumor microenvironment to neurofibroma tumorigenesis, *J. Clin. Invest.* 128 (7) (2018) 2848–2861.
- [46] D.R. Dufour, J.A. Lott, F.S. Nolte, D.R. Gretch, R.S. Koff, L.B. Seeff, Diagnosis and monitoring of hepatic injury. I. Performance characteristics of laboratory tests, *Clin. Chem.* 46 (12) (2000) 2027–2049.
- [47] E.G. Giannini, R. Testa, V. Savarino, Liver enzyme alteration: a guide for clinicians, *CMAJ (Can. Med. Assoc. J.)* 172 (3) (2005) 367–379.
- [48] B. Tian, Q. Wang, Q. Su, W. Feng, F. Li, In vivo biodistribution and toxicity assessment of triplet-triplet annihilation-based upconversion nanocapsules, *Biomaterials* 112 (2017) 10–19.
- [49] M. Quarta, M. Cromie, R. Chacon, J. Blonigan, V. Garcia, I. Akimenko, M. Hamer, P. Paine, M. Stok, J.B. Shrager, T.A. Rando, Bioengineered constructs combined with exercise enhance stem cell-mediated treatment of volumetric muscle loss, *Nat. Commun.* 8 (2017) 15613.
- [50] B.T. Corona, J.C. Rivera, J.G. Owens, J.C. Wenke, C.R. Rathbone, Volumetric muscle loss leads to permanent disability following extremity trauma, *J. Rehabil. Res. Dev.* 52 (7) (2015).
- [51] J.M. Grasman, M.J. Zayas, R.L. Page, G.D. Pins, Biomimetic scaffolds for regeneration of volumetric muscle loss in skeletal muscle injuries, *Acta Biomater.* 25 (2015) 2–15.
- [52] J. Passipieri, H. Baker, M. Siriwardane, M.D. Ellenburg, M. Vadhavkar, J.M. Saul, S. Tomblin, L. Burnett, G.J. Christ, Keratin hydrogel enhances in vivo skeletal muscle function in a rat model of volumetric muscle loss, *Tissue Eng.* 23 (11–12) (2017) 556–571.
- [53] J.T. Kim, B.M. Kasukonis, L.A. Brown, T.A. Washington, J.C. Wolchok, Recovery from volumetric muscle loss injury: a comparison between young and aged rats, *Exp. Gerontol.* 83 (2016) 37–46.
- [54] B.T. Corona, C.L. Ward, H.B. Baker, T.J. Walters, G.J. Christ, Implantation of in vitro tissue engineered muscle repair constructs and bladder acellular matrices partially restore in vivo skeletal muscle function in a rat model of volumetric muscle loss injury, *Tissue Eng.* 20 (3–4) (2014) 705–715.
- [55] E. Hill, T. Boontheekul, D.J. Mooney, Regulating activation of transplanted cells controls tissue regeneration, *Proc. Natl. Acad. Sci. USA* 103 (8) (2006) 2494–2499.
- [56] M. Yeo, G. Kim, Electrohydrodynamic-direct-printed cell-laden microfibrillar structure using alginate-based bioink for effective myotube formation, *Carbohydr. Polym.* 272 (2021) 118444.
- [57] G. Liu, R.A. Paretta, R. Wu, Y. Shi, X. Zhou, H. Liu, C. Deng, X. Sun, A. Atala, E. C. Opara, Skeletal myogenic differentiation of urine-derived stem cells and angiogenesis using microbeads loaded with growth factors, *Biomaterials* 34 (4) (2013) 1311–1326.
- [58] H. Baker, J. Passipieri, M. Siriwardane, M.D. Ellenburg, M. Vadhavkar, C. R. Bergman, J.M. Saul, S. Tomblin, L. Burnett, G.J. Christ, Cell and growth factor-loaded keratin hydrogels for treatment of volumetric muscle loss in a mouse model, *Tissue Eng.* 23 (11–12) (2017) 572–584.
- [59] W. Kim, C.H. Jang, G.H. Kim, A myoblast-laden collagen bioink with fully aligned Au nanowires for muscle-tissue regeneration, *Nano Lett.* 19 (12) (2019) 8612–8620.
- [60] V. Kroehne, I. Heschel, F. Schügner, D. Lasrich, J. Bartsch, H. Jockusch, Use of a novel collagen matrix with oriented pore structure for muscle cell differentiation in cell culture and in grafts, *J. Cell Mol. Med.* 12 (5a) (2008) 1640–1648.
- [61] C. Rhim, D.A. Lowell, M.C. Reedy, D.H. Slentz, S.J. Zhang, W.E. Kraus, G. A. Truskey, Morphology and ultrastructure of differentiating three-dimensional mammalian skeletal muscle in a collagen gel, *Muscle & Nerve, Official Journal of the American Association of Electrodiagnostic Medicine* 36 (1) (2007) 71–80.
- [62] L.A. MacQueen, C.G. Alver, C.O. Chantre, S. Ahn, L. Cera, G.M. Gonzalez, B. O'Connor, D.J. Drennan, M.M. Peters, S.E. Motta, J.F. Zimmerman, K. Parker, Muscle tissue engineering in fibrous gelatin: implications for meat analogs, *NPJ Sci Food* 3 (2019) 20.
- [63] K. Elkhoury, M. Morsink, Y. Tahri, C. Kahn, F. Cleymand, S.R. Shin, E. Arab-Tehrany, L. Sanchez-Gonzalez, Synthesis and characterization of C2C12-laden gelatin methacryloyl (GelMA) from marine and mammalian sources, *Int. J. Biol. Macromol.* 183 (2021) 918–926.
- [64] J.P. Quint, M. Samandari, L. Abbasi, E. Mollocana, C. Rinoldi, A. Mostafavi, A. Tamayol, Nanoengineered myogenic scaffolds for skeletal muscle tissue engineering, *Nanoscale* 14 (3) (2022) 797–814.
- [65] F. Velasco-Mallorquí, J.M. Fernández-Costa, L. Neves, J. Ramón-Azcón, New volumetric CNT-doped gelatin-cellulose scaffolds for skeletal muscle tissue engineering, *Nanoscale Adv.* 2 (7) (2020) 2885–2896.
- [66] Y. Guo, J. Gilbert-Honick, S.M. Somers, H.-Q. Mao, W.L. Grayson, Modified cell-electrospinning for 3D myogenesis of C2C12s in aligned fibrin microfibril bundles, *Biochem. Biophys. Res. Commun.* 516 (2) (2019) 558–564.
- [67] Ö. Lalegül-Ülker, Ş. Şeker, A.E. Elçin, Y.M. Elçin, Encapsulation of bone marrow-MSCs in PRP-derived fibrin microbeads and preliminary evaluation in a volumetric muscle loss injury rat model: modular muscle tissue engineering, *Artificial Cells, Nanomedicine, and Biotechnology* 47 (1) (2019) 10–21.
- [68] A. Lesman, J. Koffler, R. Atlas, Y.J. Blinder, Z. Kam, S. Levenberg, Engineering vessel-like networks within multicellular fibrin-based constructs, *Biomaterials* 32 (31) (2011) 7856–7869.
- [69] N. Ziemkiewicz, G.M. Hilliard, A.J. Dunn, J. Madsen, G. Haas, J. Au, P. C. Genovese, H.M. Chauvin, C. West, A. Paoli, Laminin-111-Enriched fibrin hydrogels enhance functional muscle regeneration following trauma, *Tissue Eng.* 28 (7–8) (2022) 297–311.
- [70] D. Diekjürgen, D.W. Grainger, Polysaccharide matrices used in 3D in vitro cell culture systems, *Biomaterials* 141 (2017) 96–115.
- [71] Q. Yang, J. Peng, H. Xiao, X. Xu, Z. Qian, Polysaccharide hydrogels: functionalization, construction and served as scaffold for tissue engineering, *Carbohydr. Polym.* 278 (2022) 118952.
- [72] T. Zhu, J. Mao, Y. Cheng, H. Liu, L. Lv, M. Ge, S. Li, J. Huang, Z. Chen, H. Li, Recent progress of polysaccharide-based hydrogel interfaces for wound healing and tissue engineering, *Adv. Mater. Interfac.* 6 (17) (2019) 1900761.
- [73] D.F. Coutinho, S.V. Sant, H. Shin, J.T. Oliveira, M.E. Gomes, N.M. Neves, A. Khademhosseini, R.L. Reis, Modified Gellan Gum hydrogels with tunable physical and mechanical properties, *Biomaterials* 31 (29) (2010) 7494–7502.
- [74] B. Gupta, M. Tummalapalli, B. Deepura, M. Alam, Preparation and characterization of in-situ crosslinked pectin-gelatin hydrogels, *Carbohydr. Polym.* 106 (2014) 312–318.
- [75] J.T. Koivisto, T. Joki, J.E. Parraga, R. Pääkkönen, L. Ylä-Outinen, L. Salonen, I. Jönkkäri, M. Peltola, T.O. Ihalainen, S. Narkilahti, Bioamine-crosslinked gellan gum hydrogel for neural tissue engineering, *Biomed. Mater.* 12 (2) (2017) 025014.
- [76] E.R. Morris, K. Nishinari, M. Rinaudo, Gelation of gellan—a review, *Food Hydrocolloids* 28 (2) (2012) 373–411.
- [77] S.C. Neves, D.B. Gomes, A. Sousa, S.J. Bidarra, P. Petrini, L. Moroni, C.C. Barrias, P.L. Granja, Biofunctionalized pectin hydrogels as 3D cellular microenvironments, *J. Mater. Chem. B* 3 (10) (2015) 2096–2108.
- [78] F.R. Tentor, J.H. de Oliveira, D.B. Scariot, D. Lazarin-Bidoia, E.G. Bonafe, C. V. Nakamura, S.A. Venter, J.P. Monteiro, E.C. Muniz, A.F. Martins, Scaffolds based on chitosan/pectin thermosensitive hydrogels containing gold nanoparticles, *Int. J. Biol. Macromol.* 102 (2017) 1186–1194.
- [79] C. Lee, J. Shin, J.S. Lee, E. Byun, J.H. Ryu, S.H. Um, D.-I. Kim, H. Lee, S.-W. Cho, Bioinspired, calcium-free alginate hydrogels with tunable physical and mechanical properties and improved biocompatibility, *Biomacromolecules* 14 (6) (2013) 2004–2013.
- [80] M.W. Rahman, M.T. Arafat, Gellan and xanthan-based nanocomposites for tissue engineering, *Polysaccharide-Based Nanocomposites for Gene Delivery and Tissue Engineering* (2021) 155–190. Elsevier.
- [81] Y. Song, K. Joo, J.H. Seo, Evaluation of mechanical and thermal properties of hydroxyapatite-levan composite bone graft, *Biotechnol. Bioproc. Eng.* 26 (2) (2021) 201–207.
- [82] Y. Tang, M. Hu, F. Tang, R. Huang, H. Wang, D. Wu, P. Lan, Easily-injectable shear-thinning hydrogel provides long-lasting submucosal barrier for gastrointestinal endoscopic surgery, *Bioact. Mater.* 15 (2022) 44–52.
- [83] A.J. Engler, M.A. Griffin, S. Sen, C.G. Bonnemant, H.L. Sweeney, D.E. Discher, Myotubes differentiate optimally on substrates with tissue-like stiffness: pathological implications for soft or stiff microenvironments, *J. Cell Biol.* 166 (6) (2004) 877–887.
- [84] A.J. Engler, S. Sen, H.L. Sweeney, D.E. Discher, Matrix elasticity directs stem cell lineage specification, *Cell* 126 (4) (2006) 677–689.
- [85] U.S.K. Madduma-Bandarage, S.V. Madihally, Synthetic hydrogels: synthesis, novel trends, and applications, *J. Appl. Polym. Sci.* 138 (19) (2021).
- [86] Y. Huang, M. Zhong, F.K. Shi, X.Y. Liu, Z.J. Tang, Y.K. Wang, Y. Huang, H.Q. Hou, X.M. Xie, C.Y. Zhi, An intrinsically stretchable and compressible supercapacitor containing a polyacrylamide hydrogel electrolyte, *Angew. Chem., Int. Ed.* 56 (31) (2017) 9141–9145.
- [87] X.Y. Ren, C. Huang, L.J. Duan, B.J. Liu, L.J. Bu, S. Guan, J.L. Hou, H.X. Zhang, G. H. Gao, Super-tough, ultra-stretchable and strongly compressive hydrogels with core-shell latex particles inducing efficient aggregation of hydrophobic chains, *Soft Matter* 13 (18) (2017) 3352–3358.
- [88] T. Lin, Q.W. Bai, J. Peng, L. Xu, J.Q. Li, M. Zhai, One-step radiation synthesis of agarose/polyacrylamide double-network hydrogel with extremely excellent mechanical properties, *Carbohydr. Polym.* 200 (2018) 72–81.
- [89] H.X. Zhang, W.B. Niu, S.F. Zhang, Extremely stretchable, sticky and conductive double-network ionic hydrogel for ultra-stretchable and compressible supercapacitors, *Chem. Eng. J.* 387 (2020).
- [90] Z.Z. Liu, J. Liu, J.M. Zhang, B.X. Zheng, X.L. Ren, Y.J. Long, L.M. Fang, R.X. Ou, T. Liu, Q.W. Wang, Highly compressible hydrogel sensors with synergistic long-lasting moisture, extreme temperature tolerance and strain-sensitivity properties, *Mater. Chem. Front.* 4 (11) (2020) 3319–3327.
- [91] H. Fu, F.F. Wang, Z. Cao, L. Liu, G.C. Zhu, J.M. Yao, J. Militky, J. Wiener, Super tough, stretchable and transparent ionic conductive hydrogel for flexible sensor with excellent temperature tolerance, *React. Funct. Polym.* 186 (2023).
- [92] K. Huang, Y. Wu, J. Liu, G. Chang, X. Pan, X. Weng, Y. Wang, M. Lei, A double-layer carbon nanotubes/polyvinyl alcohol hydrogel with high stretchability and

- compressibility for human motion detection, *Engineered Science* 17 (2022) 319–327.
- [93] Y. Wang, J. Liu, Y. Feng, N. Nie, M. Hu, J. Wang, G. Pan, J. Zhang, Y. Huang, An intrinsically stretchable and compressible Zn-air battery, *Chem. Commun.* 56 (35) (2020) 4793–4796.
- [94] J.R. Xavier, T. Thakur, P. Desai, M.K. Jaiswal, N. Sears, E. Cosgriff-Hernandez, R. Kaunas, A.K. Gaharwar, Bioactive nanoengineered hydrogels for bone tissue engineering: a growth-factor-free approach, *ACS Nano* 9 (3) (2015) 3109–3118.
- [95] B.C. Liu, Y. Wang, Y. Miao, X.Y. Zhang, Z.X. Fan, G. Singh, X.Y. Zhang, K.G. Xu, B. Y. Li, Z.Q. Hu, M. Xing, Hydrogen bonds autonomously powered gelatin methacrylate hydrogels with super-elasticity, self-heal and underwater self-adhesion for sutureless skin and stomach surgery and E-skin, *Biomaterials* 171 (2018) 83–96.
- [96] B.P. Partlow, C.W. Hanna, J. Rnjak-Kovacina, J.E. Moreau, M.B. Applegate, K. A. Burke, B. Marelli, A.N. Mitropoulos, F.G. Omenetto, D.L. Kaplan, Highly tunable elastomeric silk biomaterials, *Adv. Funct. Mater.* 24 (29) (2014) 4615–4624.
- [97] Y.N. Zhang, R.K. Avery, Q. Vallmajo-Martin, A. Assmann, A. Vegh, A. Memic, B. D. Olsen, N. Annabi, A. Khademhosseini, A highly elastic and rapidly crosslinkable elastin-like polypeptide-based hydrogel for biomedical applications, *Adv. Funct. Mater.* 25 (30) (2015) 4814–4826.
- [98] M.I. Giannotti, M. Rinaudo, G.J. Vancso, Force spectroscopy of hyaluronan by atomic force microscopy: from hydrogen-bonded networks toward single-chain behavior, *Biomacromolecules* 8 (9) (2007) 2648–2652.
- [99] M. Rinaudo, Non-covalent interactions in polysaccharide systems, *Macromol. Biosci.* 6 (8) (2006) 590–610.
- [100] I. Sakurada, K. Kaji, Relation between polymer conformation and elastic modulus of crystalline region of polymer, *J. Polym. Sci., Polym. Symp.* (31) (1970) 57.
- [101] W.K. Zhang, Q.B. Xu, S. Zou, H.B. Li, W.Q. Xu, X. Zhang, Z.Z. Shao, M. Kudera, H. E. Gaub, Single-molecule force spectroscopy on Bombyx mori silk fibroin by atomic force microscopy, *Langmuir* 16 (9) (2000) 4305–4308.
- [102] C.M. Madl, S.C. Heilshorn, H.M. Blau, Bioengineering strategies to accelerate stem cell therapeutics, *Nature* 557 (7705) (2018) 335–342.
- [103] M. Smoak, A. Mikos, Advances in biomaterials for skeletal muscle engineering and obstacles still to overcome, *Materials today bio* 7 (2020) 100069.
- [104] X. Chen, W. Du, Z. Cai, S. Ji, M. Dwivedi, J. Chen, G. Zhao, J. Chu, Uniaxial stretching of cell-laden microfibers for promoting C2C12 myoblasts alignment and myofibers formation, *ACS Appl. Mater. Interfaces* 12 (2) (2019) 2162–2170.
- [105] T. Sahana, P. Rekha, A novel exopolysaccharide from marine bacterium *Pantoea* sp. YU16-S3 accelerates cutaneous wound healing through Wnt/ β -catenin pathway, *Carbohydr. Polym.* 238 (2020) 116191.
- [106] R. Seyedmahmoud, B. Çelebi-Saltik, N. Barros, R. Nasiri, E. Banton, A. Shamloo, N. Ashammakhi, M.R. Dokmeci, S. Ahadian, Three-dimensional bioprinting of functional skeletal muscle tissue using gelatin methacryloyl-alginate bioinks, *Micromachines* 10 (10) (2019) 679.
- [107] J.A. Rowley, D.J. Mooney, Alginate type and RGD density control myoblast phenotype, *J. Biomed. Mater. Res.: An Official Journal of The Society for Biomaterials*, The Japanese Society for Biomaterials, and The Australian Society for Biomaterials and the Korean Society for Biomaterials 60 (2) (2002) 217–223.
- [108] J. Ge, K. Liu, W. Niu, M. Chen, M. Wang, Y. Xue, C. Gao, P.X. Ma, B. Lei, Gold and gold-silver alloy nanoparticles enhance the myogenic differentiation of myoblasts through p38 MAPK signaling pathway and promote in vivo skeletal muscle regeneration, *Biomaterials* 175 (2018) 19–29.
- [109] I. Jun, S. Jeong, H. Shin, The stimulation of myoblast differentiation by electrically conductive sub-micron fibers, *Biomaterials* 30 (11) (2009) 2038–2047.
- [110] J.S. Choi, H.I. Yoon, K.S. Lee, Y.C. Choi, S.H. Yang, I.-S. Kim, Y.W. Cho, Exosomes from differentiating human skeletal muscle cells trigger myogenesis of stem cells and provide biochemical cues for skeletal muscle regeneration, *J. Contr. Release* 222 (2016) 107–115.
- [111] J. Kim, B. Kasukonis, K. Roberts, G. Dunlap, L. Brown, T. Washington, J. Wolchok, Graft alignment impacts the regenerative response of skeletal muscle after volumetric muscle loss in a rat model, *Acta Biomater.* 105 (2020) 191–202.
- [112] S. Ostrovidov, S. Salehi, M. Costantini, K. Suthiwanich, M. Ebrahimi, R. B. Sadeghian, T. Fujie, X. Shi, S. Cannata, C. Gargioli, A. Tamayol, M.R. Dokmeci, G. Orive, W. Swieszkowski, A. Khademhosseini, 3D bioprinting in skeletal muscle tissue engineering, *Small* 15 (24) (2019) e1805530.
- [113] J. Gilbert-Honick, S.R. Iyer, S.M. Somers, H. Takasuka, R.M. Lovering, K. R. Wagner, H.Q. Mao, W.L. Grayson, Engineering 3D skeletal muscle primed for neuromuscular regeneration following volumetric muscle loss, *Biomaterials* 255 (2020) 120154.
- [114] Y.J. Choi, Y.J. Jun, D.Y. Kim, H.G. Yi, S.H. Chae, J. Kang, J. Lee, G. Gao, J. S. Kong, J. Jang, W.K. Chung, J.W. Rhie, D.W. Cho, A 3D cell printed muscle construct with tissue-derived bioink for the treatment of volumetric muscle loss, *Biomaterials* 206 (2019) 160–169.
- [115] C.S. Russell, A. Mostafavi, J.P. Quint, A.C. Panayi, K. Baldino, T.J. Williams, J. G. Daubendiek, V. Hugo Sánchez, Z. Bonick, M. Trujillo-Miranda, In situ printing of adhesive hydrogel scaffolds for the treatment of skeletal muscle injuries, *ACS Appl. Bio Mater.* 3 (3) (2020) 1568–1579.
- [116] T. Ben-Arye, Y. Shandalov, S. Ben-Shaul, S. Landau, Y. Zagury, I. Ianovici, N. Lavon, S. Levenberg, Textured soy protein scaffolds enable the generation of three-dimensional bovine skeletal muscle tissue for cell-based meat, *Nat Food* 1 (4) (2020).
- [117] N.R. Rubio, N. Xiang, D.L. Kaplan, Plant-based and cell-based approaches to meat production, *Nat. Commun.* 11 (1) (2020).
- [118] L. Thorrez, H. Vandenburgh, Challenges in the quest for ‘clean meat’, *Nat. Biotechnol.* 37 (3) (2019) 215–216.
- [119] S.R. Sindhu Raveendran, B.P. Binod Parameswaran, S. Ummalyma, A.A. Amith Abraham, A. Mathew, A.M. Aravind Madhavan, S.R. Sharrel Rebello, A.P. Ashok Pandey, Applications of Microbial Enzymes in Food Industry, 2018.
- [120] M. Bhat, Cellulases and related enzymes in biotechnology, *Biotechnol. Adv.* 18 (5) (2000) 355–383.
- [121] X. Wu, B.T. Corona, X. Chen, T.J. Walters, A standardized rat model of volumetric muscle loss injury for the development of tissue engineering therapies, *BioResearch Open Access* 1 (6) (2012) 280–290.